minerals

MDPI

Article

The Petrogenesis of the Earliest Early Cretaceous Subvolcanic Granitic Intrusions in the Huoluotai Area, Northern Great Xing'an Range: Implications for the Regional Compression–Extension Tectonic Transition in the Eastern Mongol–Okhotsk Tectonic Domain

Gantian Li [1,2], Bile Li [1,*], Zhibin Li [3], Lixiang Zhao [1] and Xiaowei Li [3]

[1] College of Earth Sciences, Jilin University, Changchun 130061, China; lgt910619@163.com (G.L.); lxzhao25@mails.jlu.edu.cn (L.Z.)
[2] Zhongze Holding Group Co., Ltd., Beijing 100020, China
[3] No. 1 Geological Survey Institute of Jilin Province, Changchun 130031, China; splzb@163.com (Z.L.); lxw101107@163.com (X.L.)
* Correspondence: libl@jlu.edu.cn

Abstract

Late Mesozoic magmatic rocks are widely exposed in the northern Great Xing'an Range, a key region recording Phanerozoic crustal growth along the eastern Central Asian Orogenic Belt (CAOB). This study integrates petrology, LA–ICP–MS zircon U–Pb geochronology, zircon Hf isotopes, and whole-rock geochemistry for Late Mesozoic granitic subvolcanic intrusions in the Huoluotai area, northern Great Xing'an Range. Zircon U–Pb dating yields crystallization ages of 143.4 ± 1.2 Ma for the felsite and 138.8 ± 2.0 Ma for the rhyolite porphyry, documenting early Early Cretaceous emplacement. Geochemical data reveals that the investigated felsite and rhyolite porphyry exhibit high SiO_2, K_2O and total alkali ($K_2O + Na_2O$) contents, coupled with low MgO, $Mg^{\#}$, Ni, Sr and Yb values, and thus belong to shoshonitic I-type granites. The samples are enriched in large-ion lithophile elements (LILIs; e.g., Rb, K, U) and light rare earth elements (LREEs), with depletion of high-field-strength elements (HFSEs; e.g., Nb, Ta, P, Ti) and heavy rare earth elements (HREEs), accompanied by pronounced negative Eu anomalies, typical of crust-derived magmas. Zircon $\varepsilon_{Hf}(t)$ values range from −2.25 to +1.57 for the felsite (T_{DM2} = 1092–1334 Ma) and −0.65 to +3.58 for the rhyolite porphyry (T_{DM2} = 960–1229 Ma). Zircon Hf isotopic features demonstrate that the primary magmas were mainly derived from Mesoproterozoic juvenile crust, accompanied by variable mixing with ancient sialic crustal components. The felsite and rhyolite porphyry formed in a post-collisional extensional setting, constraining the final closure of the eastern Mongol–Okhotsk Ocean to earlier than ~144 Ma. By contrast, Late Jurassic (150–146 Ma) Mo-mineralization-related granitoids in this area are Na-rich adakites with high Sr and low Yb, generated during oceanic subduction. The remarkable geochemical transition from 150–146 Ma subduction-related Na-rich adakites to 143–139 Ma post-collisional K-rich granites restricts a tectonic transition from compression to extension at ~145 Ma in the northern Great Xing'an Range.

Keywords: northern Great Xing'an Range; Mongol–Okhotsk Ocean; earliest Early Cretaceous; subvolcanic granitic intrusions; highly fractionated I-type granites; tectonic transition from compression to extension

Check for updates

Academic Editors: Jean-Michel Lafon and Dmitry Konopelko

Received: 28 July 2026
Revised: 27 August 2026
Accepted: 30 August 2026
Published: 31 August 2026

Copyright: © 2026 by the authors. Licensee MDPI, Basel, Switzerland. This article is an open access article distributed under the terms and conditions of the Creative Commons Attribution (CC BY) license.

1. Introduction

The Central Asian Orogenic Belt (CAOB) is the largest and most complex accretionary orogen preserved worldwide [1,2]. Located in the eastern CAOB, the Great Xing'an Range has undergone superposition and transition of three major tectonic domains since the Phanerozoic, namely the Paleo-Asian Ocean, Mongol–Okhotsk Ocean and Paleo-Pacific domains [3]. The timing and spatial extent of tectonic transitions among these three domains remain controversial and constitute a long-standing research hotspot. Accumulated evidence demonstrates that the Paleo-Asian Ocean domain of the CAOB underwent a protracted evolutionary history from the Paleozoic to Early Mesozoic, including multi-directional subduction, continental marginal accretion, soft collision and microcontinent amalgamation, followed by post-collisional extension and intracontinental orogeny in response to Gondwana assembly [4–7]. Discrete microcontinental blocks within this orogen are bounded by major faults and ancient suture zones. Since the Mesozoic, the eastern segment of the CAOB has been superimposed and reworked by the Mongol–Okhotsk Ocean and Paleo-Pacific Ocean tectonic domains, resulting in widespread Late Mesozoic granites and volcanic rocks [3,7].

Traditionally, the Mongol–Okhotsk Ocean is divided into western and eastern segments by the longitude of 120° E, and the western segment is suggested to have closed during the Early–Middle Jurassic [8,9]. Nevertheless, the evolutionary process of the eastern Mongol–Okhotsk Ocean remains highly controversial. In particular, the timing, spatial pattern and geodynamic mechanism of the regional tectonic regime transition from compressional subduction to post-collisional extension, as well as its genetic link to ocean closure, constitute long-standing core issues in regional geological research, with three major viewpoints proposed: (1) Tectonic transition at the latest Jurassic–earliest Cretaceous (~145 Ma) [10–12]: Tectonostratigraphic analysis of the Junggar Basin shows that intense folding and uplift affected the eastern and northeastern parts of the basin at the Jurassic–Cretaceous transition, accompanied by abrupt shifts in depositional systems and widespread coarse-grained clastic infill. This prominent intraplate deformation event has been interpreted as a far-field tectonic response to the final closure of the eastern Mongol–Okhotsk Ocean [11]. In addition, the transition from marine-continental foreland deposits to continental molasse sequences in the Upper Amur Basin [12], the abrupt termination of subduction-related porphyry Mo mineralization at ca. 146 Ma, and the geochemical shift from compressional adakitic magmatism to extensional highly fractionated granitic magmatism in the northern Great Xing'an Range collectively corroborate this timing. (2) Post-collisional extension at 130–120 Ma in the Early Cretaceous [13]: Paleomagnetic data indicate that the Siberian and North China cratons did not complete their suturing in the eastern segment until 130–120 Ma [13], and the widespread 130–120 Ma A-type granites and bimodal volcanic rocks across the Great Xing'an Range have been interpreted as products of post-collisional lithospheric delamination. (3) Final ocean closure at ~98 Ma in the earliest Late Cretaceous [14]: This hypothesis proposes that the Mongol–Okhotsk Ocean did not close completely until ~98 Ma, based on the tectonic transformation from extension to compression in Northeast Asia and the inferred accretion of an oceanic plateau within the ocean basin [14].

The northern Great Xing'an Range is extensively covered by volcanic rocks and granites formed during the earliest Early Cretaceous, whereas their tectonic setting remains highly controversial. Two competing models have been proposed: (1) magmatism was triggered by subduction of the Paleo-Pacific plate [15,16]; and (2) magmatic activities were dominated by post-collisional extension following the closure of the Mongol–Okhotsk Ocean [3,17,18]. Dykes and subvolcanic intrusions serve as sensitive petrological tracers for tectonic regime transitions and crust–mantle dynamics, as their emplacement is directly

controlled by regional stress reorganization and deep geodynamic processes [19]. In the northern Great Xing'an Range, accumulated geochronological data have documented a prominent episode of dyke and subvolcanic magmatism during the earliest Early Cretaceous (ca. 145–135 Ma), such as the Hulalin quartz porphyry (144.9 Ma) [20], Huoluotai diorite porphyrite (142.0 Ma) [21], and Qilibin trachyandesite of the Manitu Formation (142.2–141.0 Ma) [22], define a continuous magmatic event spanning the Late Jurassic–Early Cretaceous boundary. Geochemically, these earliest Early Cretaceous felsic dykes and subvolcanic rocks are characterized by high SiO_2 and K_2O contents, low Sr and Yb abundances, pronounced negative Eu anomalies and highly fractionated I-type affinities [20], which are distinctly different from the Late Jurassic (150–146 Ma) Na-rich adakitic ore-related porphyries formed in a compressional subduction setting [17]. Nevertheless, previous studies have predominantly focused on large-scale volcanic successions and deep-seated plutonic bodies. Systematic petrogenetic and isotopic investigations of earliest Early Cretaceous felsic subvolcanic intrusions, such as felsite and rhyolite porphyry, remain scarce. The precise timing of post-collisional extension initiation and the detailed magmatic evolutionary sequence across the ~145 Ma tectonic transition still require further refinement.

This study focuses on subvolcanic felsic intrusions from the Huoluotai area in the northern Great Xing'an Range. We present integrated zircon U–Pb geochronology, whole-rock major and trace element geochemistry, and in situ zircon Hf isotopic data to precisely constrain the emplacement ages of these granitic intrusions and unravel their petrogenesis, magma source characteristics and geodynamic setting. Combined with the lithological assemblages and spatial–temporal variations of Late Mesozoic magmatic rocks across the northern Great Xing'an Range, we further constrain the timing of tectonic transition and post-orogenic extensional processes. Our results provide critical insights into Mesozoic magmatic evolution and tectonic regime transition in the eastern CAOB.

2. Geological Setting and Sample Description

The Great Xing'an Range is located in the western part of Northeast China and consists of the Erguna Block, Xing'an Block and western segment of the Songnen–Zhangguangcai Range Block (Figure 1a) [4,23]. The northern Great Xing'an Range is mainly composed of the Erguna Block and the northern parts of Xing'an blocks, and the study area is situated in the central uplift belt of the Emuer Mountain within the Erguna Block [17]. Exposed stratigraphic units in the northern Erguna Block consist of metamorphic rocks of the Mesoproterozoic Xinghuadukou Group, low-grade metamorphic rocks of the Lower Cambrian Ergunahe Formation, and Paleozoic–Mesozoic sedimentary sequences. Igneous rocks consist predominantly of Early Paleozoic granitoids and Mesozoic magmatic rocks. Tectonically, faults striking NE, sub-EW and NW are well developed (Figure 1b).

The Huoluotai area is located approximately 50 km southwest of Mohe County and tectonically lies in the northern Erguna Block. Exposed strata consist of the Mesoproterozoic Xinghua Group, which is dominated by amphibolite, leptynite, gneiss and schist, with limited outcrops mostly preserved as residual blocks. Jurassic volcanic–sedimentary sequences are also developed, including the Tamulangou, Manketouebo and Baiyingaolao formations, which are dominated by intermediate-felsic volcanic and volcaniclastic rocks. Porphyritic monzogranite is widely exposed as dominant intrusions in the study area. Other intrusive rocks include felsite, rhyolite porphyry, diorite porphyrite and diabase. Field observations show that the felsite occurs as small stocks and dykes, while the rhyolite porphyry mainly occurs as dykes. Both units have sharp intrusive contacts with the host porphyritic monzogranite, with weak contact metamorphic halos developed locally; they also intrude into the metamorphic rocks of the Xinghua Group in a few localities. In terms of the relative emplacement sequence, the large-scale porphyritic monzogranite formed

first, followed by the felsite and the rhyolite porphyry successively, recording multi-stage magmatic activity during the earliest Early Cretaceous.

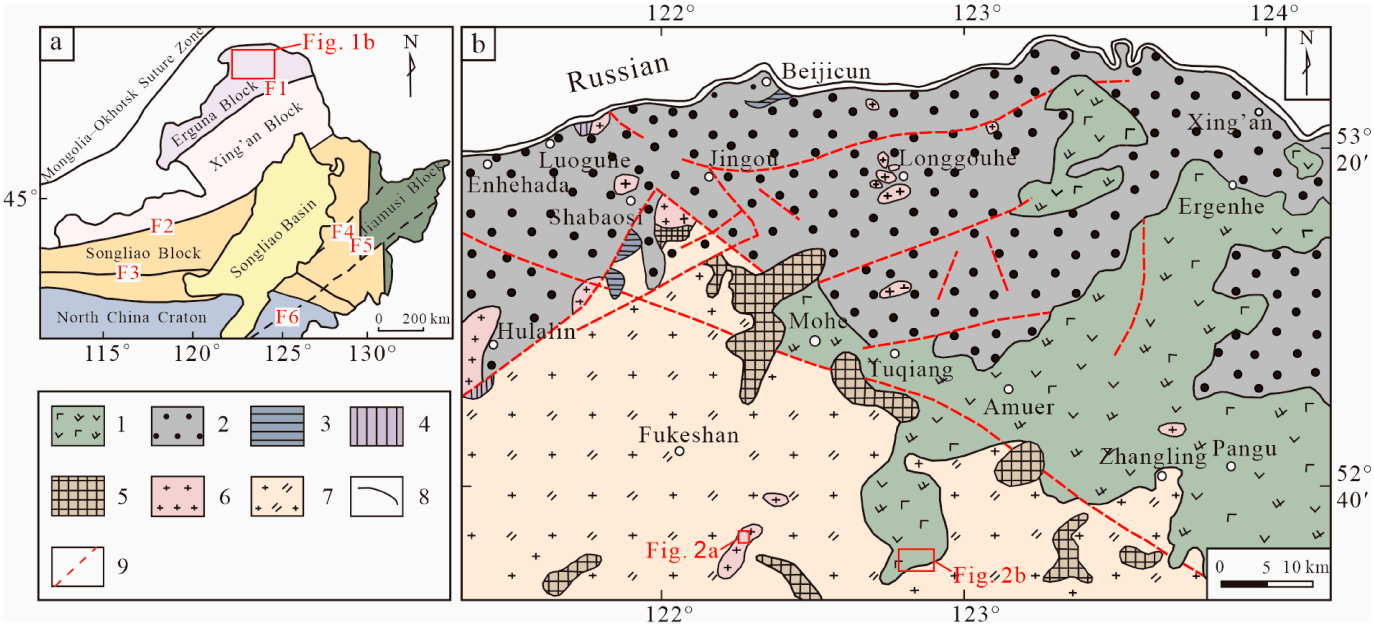


Figure 1. (**a**) Tectonic framework of Northeast China and (**b**) regional geological map of northern segment of Erguna Block [24]. 1—Mesozoic volcanic rocks; 2—Mesozoic sedimentary rocks; 3—Paleozoic sedimentary rocks; 4—Cambrian metamorphic rocks; 5—Mesoproterozoic metamorphic rocks; 6—Mesozoic granites; 7—Early Paleozoic granites; 8—Geological boundary; 9—Fault; F1—Xinlin–Xiguitu suture zone; F2—Hegenshan–Heihe suture zone; F3—Xar Moron–Changchun suture zone; F4—Yitong–Yilan fault; F5—Mudanjiang–Yilan suture zone; F6—Dunhua–Mishan fault.

In this study, six felsite samples and six rhyolite porphyry samples from the Huoluotai area were selected for systematic analysis. The felsite sample (HLT-L9) was collected from surface trench TC32-1 in the eastern part of Huoluotai area II. This felsite occurs as a small stock intruding into porphyritic monzogranite and covers an outcrop area of ~0.24 km^2, with GPS coordinates of 52°34′36″ N, 122°06′10″ E (Figure 2a). The rhyolite porphyry sample (ZK30-1) was obtained from a drill core at depths of 253.35–262.45 m in a vertical borehole ZK30-1 of Huoluotai area I. This rock also intrudes porphyritic monzogranite and its sampling site is located at 52°30′26″ N, 122°50′43″ E (Figure 2b).

The felsite exhibits yellowish-brown weathered surfaces and grayish-white fresh surfaces (Figure 3a). It possesses a felsitic texture with mineral grain sizes ranging from 0.05 to 1.00 mm. Locally, quartz and feldspar microlites form a micrographic texture, which gradually transitions to a porphyritic texture, containing 1–1.5 mm quartz phenocrysts with obvious corrosion textures. The rock is mainly composed of K-feldspar, plagioclase and quartz. Under cross-polarized light, K-feldspar generally undergoes kaolinization with cloudy surfaces and yields yellowish-white interference colors; distinct Carlsbad twins are observed on some K-feldspar. Plagioclase displays uneven sericitization and shows grayish-white to pale blue interference colors. Both feldspars develop euhedral tabular shapes and account for approximately 65 vol.% of the rock; quartz constitutes ~31 vol.%, and opaque metallic minerals occur as accessory minerals (~1 vol.%). Quartz grains show a strong preferred orientation, and feldspar crystals also display a moderate orientation (Figure 3b,c).

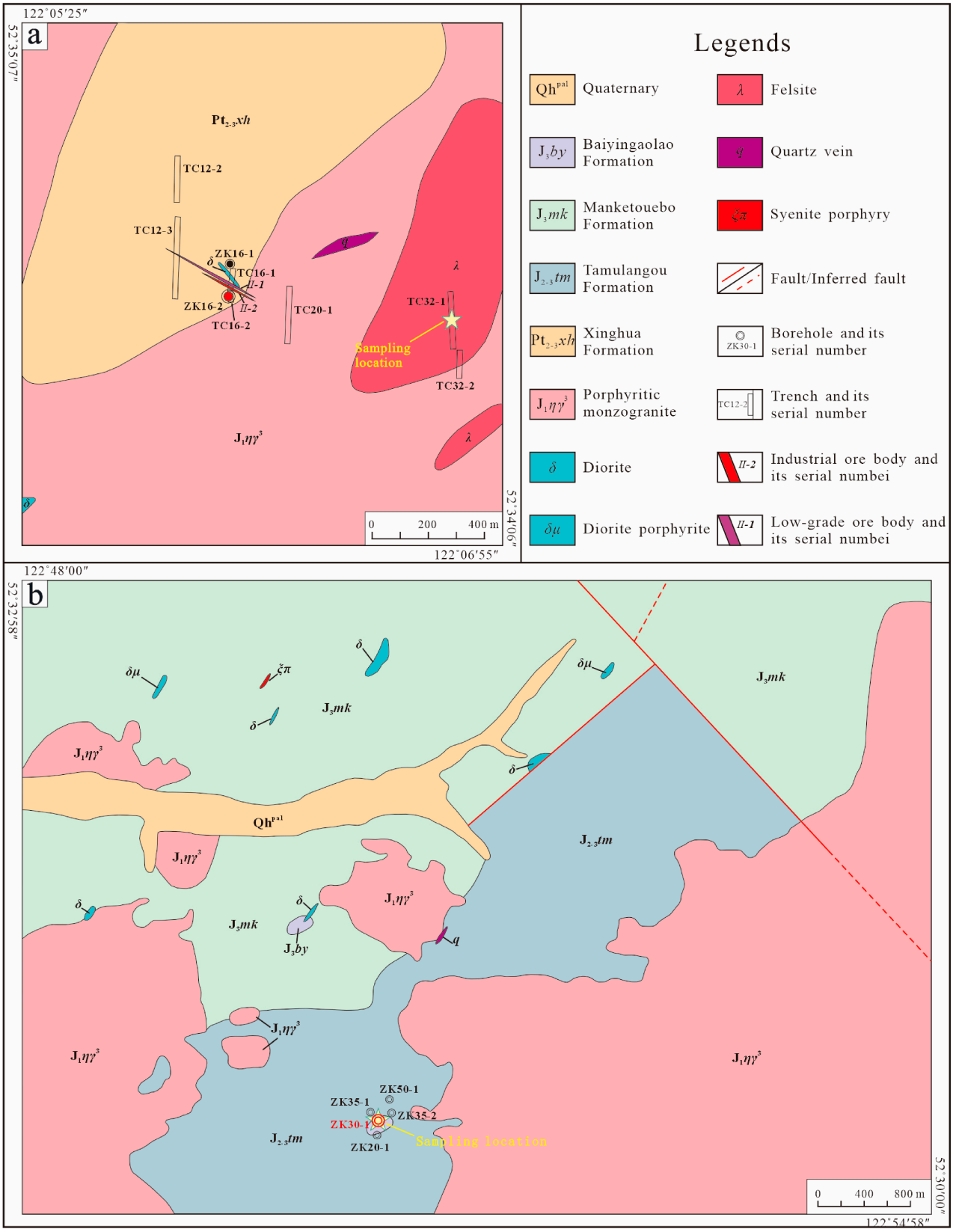


Figure 2. Geological sketch map of (**a**) segment II and (**b**) I from the Huoluotai area.

The rhyolite porphyry has pale flesh-red fresh surfaces and a typical porphyritic texture (Figure 3d). Its groundmass shows a cryptocrystalline to vitreous texture. Phenocrysts are dominated by orthoclase, albite and plagioclase with minor biotite, ranging from 1.5 to 7.7 mm and occupying about 20 vol.% of the rock. Tabular orthoclase crystals show vari-

able kaolinization and well-developed Carlsbad twins. Tabular albite is characterized by prominent Carlsbad–albite compound twins. Tabular plagioclase develops polysynthetic twins and variable degrees of sericitization. Platy biotite appears brown due to surface alterations. The groundmass is primarily composed of anhedral cryptocrystalline–vitreous quartz, with minor opaque metallic minerals (~1.5 vol.%) (Figure 3e,f).

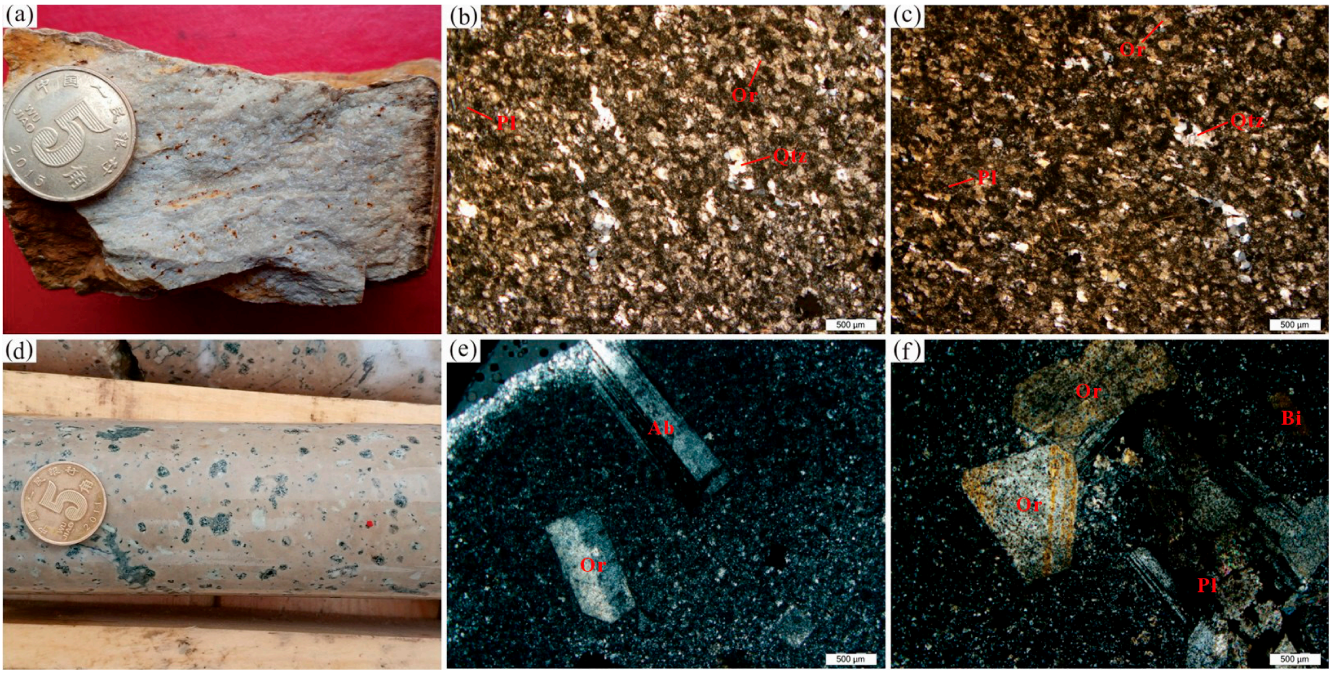


Figure 3. (**a**,**d**) Specimen photograph and (**b**,**c**,**e**,**f**) microphotograph of felsites and rhyolite porphyry from the Huoluotai area. Qtz—quartz; Or—orthoclase; Ab—albite; Pl—plagioclase; Bi—biotite.

3. Analytical Methods

3.1. Zircon U–Pb Geochronology

Zircon separation was performed at Langfang Yuheng Mineral and Rock Technical Service Co., Ltd., Langfang, China. Zircon target preparation and cathodoluminescence (CL) imaging were completed at Beijing Zhaonian Linghang Technology Co., Ltd., Beijing, China.

In situ zircon U–Pb dating was carried out by LA–ICP–MS at the Key Laboratory of Mineral Resources Evaluation in Northeast Asia, Ministry of Land and Resources, Jilin University. The laser ablation system consists of a COMPEx Pro 193 nm ArF excimer laser, Coherent LaserSystems GmbH & Co. KG, Göttingen, Germany, coupled to an Agilent 7900 ICP-MS instrument, Agilent Technologies, Santa Clara, CA, USA. The NIST SRM 610 glass (National Institute of Standards and Technology, Gaithersburg, MD, USA) was used for instrument optimization, and the standard zircon 91500 was adopted as an external standard for U–Pb isotopic calibration. Laser spot size of 32 μm with a repetition rate of 7 Hz was employed during ablation analysis. Raw analytical data were processed using the GLITTER 4.4 software package, and age calculations were performed with the Isoplot 4.15 program. All analytical results are listed in Table S1.

3.2. Major and Trace Element Analyses

Whole-rock major, trace and rare earth element analyses were conducted at Beijing Yandu Zhongshi Testing Technology Co., Ltd., Beijing, China. Twelve fresh rock samples were first crushed to centimeter-sized fragments, cleaned with purified water and dried, then pulverized to pass through a 200-mesh sieve prior to geochemical measurement.

For major element analysis, weighed powder samples were mixed with lithium tetraborate flux at a sample-to-flux ratio of 1:8 and fused into homogeneous glass beads in Pt crucibles at 1150 °C using a fusion machine. The prepared glass discs were measured by an XRF spectrometer (Zetium, Malvern Panalytical, Almelo, The Netherlands), with analytical uncertainties better than 1%.

For trace element determination, weighed 200-mesh powders were loaded into PTFE digestion bombs and dissolved in mixed HF + HNO_3. The sealed bombs were heated at 190 °C for 72 h in an oven, followed by acid evaporation and constant-volume dilution before instrumental testing. Measurements were performed on an ICP-MS instrument (M90, Analytik Jena GmbH+Co. KG, Jena, Germany). Based on certified reference material GSR-2, analytical precision is better than 5% for most elements and less than 10% for volatile and ultra-low-abundance trace elements. All analytical data are summarized in Table S2.

3.3. In Situ Zircon Lu–Hf Isotope Analysis

In situ zircon Lu–Hf isotopic measurements were carried out at the Laboratory of Continental Tectonics and Dynamics, Institute of Geology, Chinese Academy of Geological Sciences. Analyses were performed on a Neptune MC-ICP-MS equipped with a 193 nm laser ablation system, following the analytical procedures and calibration protocols described by [25]. Zircon Hf model ages were calculated using the depleted-mantle evolutionary model described by [26]. A continental crust $^{176}Lu/^{177}Hf$ ratio of 0.015 [27,28] was adopted for the calculation of two-stage Hf model ages (T_{DM2}). During the analytical session, the weighted mean $^{176}Hf/^{177}Hf$ ratio of standard zircon GJ-1 was determined to be 0.282285 ± 0.000013 (n = 35). All Hf isotopic data are listed in Table S3.

4. Analytical Results

4.1. Zircon U–Pb Dating

LA–ICP–MS zircon U–Pb isotopic dating data for the felsite and rhyolite porphyry are presented in Table S1. Zircons separated from the felsite generally have clean surfaces and predominantly euhedral to subhedral granular morphologies with straight crystal edges. Cathodoluminescence (CL) images reveal distinct magmatic oscillatory zoning (Figure 4a). These zircons range in grain size from 95 to 121 μm, with length/width ratios mostly between 1.11 and 1.78. Their measured Th and U contents vary from 161 ppm to 1608 ppm and 184 ppm to 1422 ppm, respectively, corresponding to Th/U ratios of 0.62–1.15. Zircon morphology, internal texture and high Th/U ratios collectively indicate a magmatic origin [29]. The weighted mean $^{206}Pb/^{238}U$ age of ten analyzed spots is 143.4 ± 1.2 Ma (MSWD = 0.64, n = 10; Figure 5a), corresponding to the earliest Early Cretaceous and interpreted as the crystallization age of the host felsite.

Zircons from the rhyolite porphyry display clean surfaces and are mostly euhedral to subhedral granular or prismatic crystals with perfect crystal edges. Distinct magmatic oscillatory zoning is observed under cathodoluminescence (CL; Figure 4b). The zircon grains range from 100 to 180 μm in size, and their length-to-width ratios mainly vary between 1.22 and 2.41. Analyzed spots yield Th and U concentrations of 65 ppm–267 ppm and 65 ppm–194 ppm, respectively, with Th/U ratios of 0.87–1.37. Combined zircon morphology, internal texture and Th/U ratios suggest a magmatic origin for these zircons [29]. The weighted mean $^{206}Pb/^{238}U$ age of 14 analytical spots is 138.8 ± 2.0 Ma (MSWD = 0.52, n = 14; Figure 5b), representing the crystallization age of the rhyolite porphyry and corresponding to the earliest Early Cretaceous.



Figure 4. Cathodoluminescence (CL) images of zircons of the (**a**) felsite and the (**b**) rhyolite porphyry from the Huoluotai area. (Red circle: zircon age test point; Yellow circle: Hf isotopic test point).

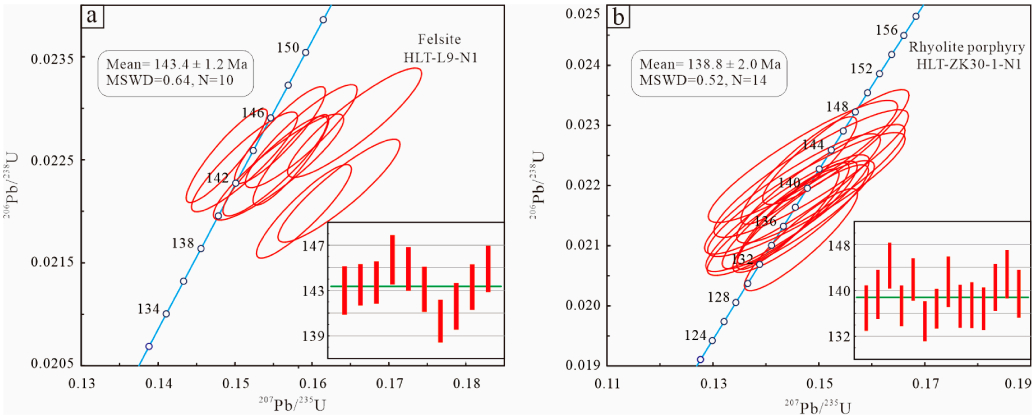


Figure 5. Concordia diagram and frequency diagram showing zircon U-Pb dating result of the (**a**) felsite and the (**b**) rhyolite porphyry from the Huoluotai area.

4.2. Whole-Rock Geochemistry

Twelve major element compositions are listed in Table S2. The felsite samples show markedly high silica concentrations, with SiO_2 ranging from 77.27% to 77.71%, and possess extremely high differentiation indices (DI = 96.10%–97.56%). These rocks are enriched in total alkalis ($K_2O + Na_2O$ = 8.39%–9.17%) and display relative K-rich, Na-poor signatures, as reflected by Na_2O contents of 2.98%–3.30%, K_2O contents of 5.19%–5.97%, and K_2O/Na_2O ratios of 1.62–1.87. Additionally, they contain low abundances of total iron, magnesium and phosphorus (TFe_2O_3 = 0.30%–0.86%, MgO = 0.10%–0.14%, P_2O_5 = 0.01%–0.02%), alongside low CaO values of 0.09%–0.10%. All felsite data points plot within the granite field on the ($Na_2O + K_2O$)–SiO_2 diagram (Figure 6a) and fall into the monzogranite domain in the Q–A–P ternary diagram (Figure 6b). The rocks have Al_2O_3 contents of 12.81%–13.10%

and an alumina saturation index (A/CNK) between 1.09 and 1.18, indicative of a weakly peraluminous character (Figure 6c). On the K_2O–SiO_2 discriminant diagram (Figure 6d), all samples are distributed in the shoshonitic series field.

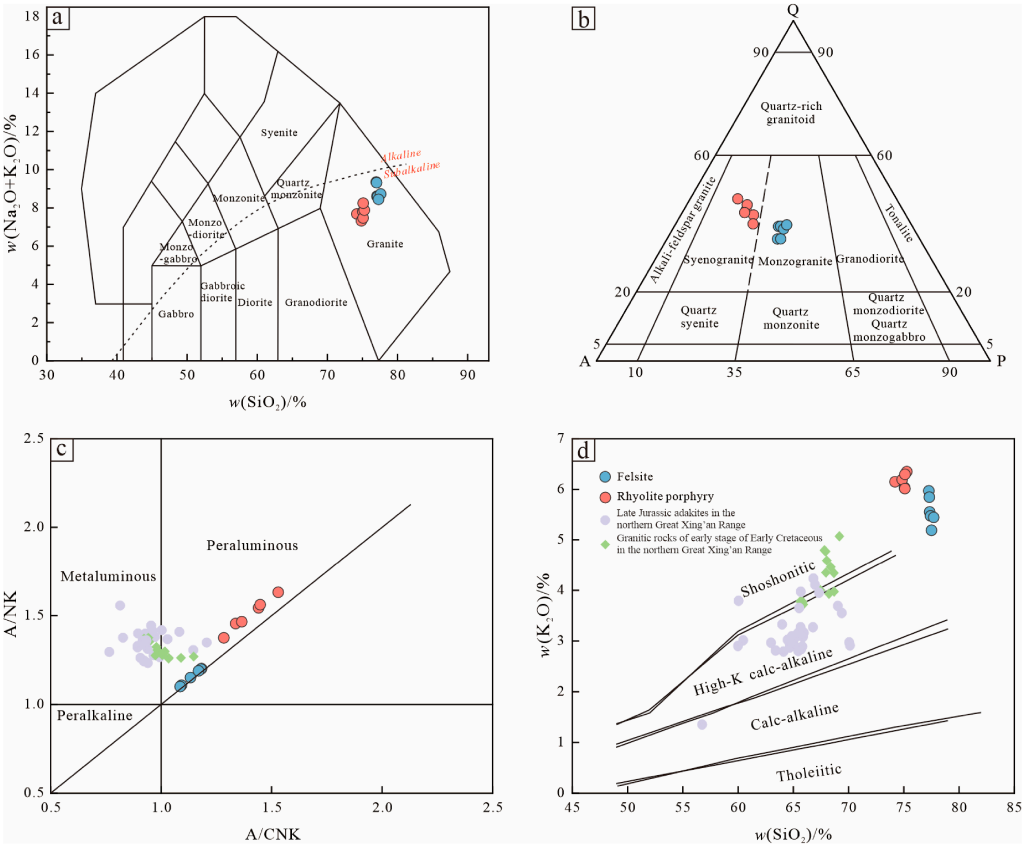


Figure 6. Discrimination diagrams of the felsite and the rhyolite porphyry from the Huoluotai area. (**a**) (Na_2O + K_2O)-SiO_2 diagram [30]; (**b**) QAP diagram [31]; (**c**) A/NK-A/CNK diagram [31] and (**d**) K_2O vs. SiO_2 diagram [32]. Data of Late Jurassic adakites in the northern Great Xing'an Range quoted from [33–35]. Data of granitic rocks from early stage of Early Cretaceous in the northern Great Xing'an Range quoted from [34,36].

The rhyolite porphyry samples are characterized by high silica contents (SiO_2 = 74.21%–75.27%) and elevated differentiation indices (DI = 89.28%–91.03%). The rocks are alkali-rich, with total alkali contents (K_2O + Na_2O) ranging from 7.33% to 8.25%, and exhibit distinct K-rich and Na-poor features (Na_2O = 1.14%–1.95%, K_2O = 6.01%–6.35%, K_2O/Na_2O = 3.23–5.45). In addition, they display low contents of total iron, magnesium, and phosphorus (TFe_2O_3 = 1.80%–2.81%, MgO = 0.30%–0.38%, P_2O_5 = 0.03%–0.04%), with CaO values of 0.31%–0.46%. All samples plot in the granite field in the (Na_2O + K_2O)–SiO_2 diagram (Figure 6a) and fall within the syenogranite domain in the Q–A–P classification diagram (Figure 6b). The rocks have Al_2O_3 contents of 13.73%–14.16% and A/CNK ratios of 1.28–1.53, indicating a peraluminous affinity (Figure 6c). Meanwhile, all samples belong to the shoshonitic series in the K_2O–SiO_2 discriminant diagram (Figure 6d).

Trace element compositions are listed in Table S2. The felsite samples exhibit low total rare earth element abundances (ΣREE = 23.78 ppm–46.22 ppm, with an average value of 38.05 ppm (n = 6), and show pronounced negative Eu anomalies (δEu = 0.43–0.52, mean = 0.48, n = 6). The rocks have LREE/HREE ratios of 9.58–15.70 and chondrite-normalized $(La/Yb)_N$ values ranging from 6.26 to 15.14. Their chondrite-normalized REE patterns are markedly right-inclined, implying strong fractionation between light and heavy

REEs, whereas heavy REEs display weak fractionation with nearly flat trends. Compared with coeval granitoids in the northern Great Xing'an Range, these felsites feature lower total REE contents and more intense negative Eu anomalies (Figure 7a). On the primitive mantle-normalized trace element spidergrams (Figure 7b), the samples are enriched in K, Rb and U, depleted in Ba and Sr, and show distinct depletion of high-field-strength elements (HFSEs: Nb, Ta, Ti).

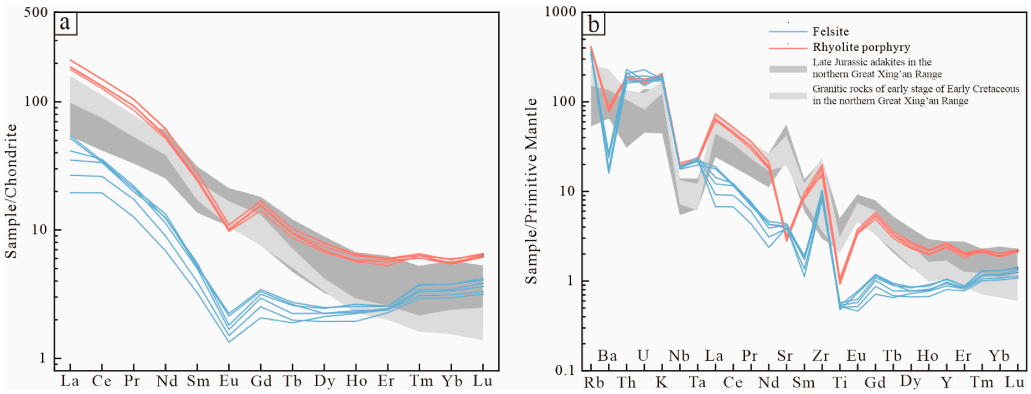


Figure 7. (**a**) Chondrite-normalized REEs and (**b**) primitive-mantle normalized multi-element diagrams of the felsite and the rhyolite porphyry from the Huoluotai area. (The normalization values are from [37]). Data sources are the same as in Figure 6.

The rhyolite porphyry samples are characterized by LREE enrichment and HREE depletion, with total rare earth element contents (ΣREE) ranging from 164 ppm to 195 ppm and prominent LREE/HREE fractionation. The samples exhibit LREE/HREE ratios of 20.31–21.85 and chondrite-normalized $(La/Yb)_N$ values of 31.45–36.49, with distinct negative Eu anomalies (δEu = 0.50–0.53). Overall, the rhyolite porphyry samples show similar REE patterns to coeval granitic rocks in the northern Great Xing'an Range but display more intense negative Eu anomalies (Figure 7a). In the primitive mantle-normalized trace element spider diagrams (Figure 7b), the rhyolite porphyry is enriched in K, Rb, and U, depleted in Sr, and exhibits significant depletion of Nb, Ta, Ti, and P.

4.3. Zircon Lu–Hf Isotope

Zircon grains from the felsite and rhyolite porphyry samples yield uniformly low $^{176}Lu/^{177}Hf$ ratios of less than 0.002 (Table S3), implying negligible radiogenic Hf accumulation via in situ Lu decay after magma emplacement and crystallization, which permits the application of zircon $^{176}Hf/^{177}Hf$ ratios to constrain petrogenesis of the pluton [38]. Zircons from the felsite have $^{176}Hf/^{177}Hf$ values ranging from 0.282624 to 0.282729, with calculated $\varepsilon_{Hf}(t)$ values varying between −2.25 and +1.57 and most data clustering around zero (Table S3). All analytical spots plot close to the chondritic evolution line on Hf isotopic diagrams (Figure 8a,b). As proposed by [39], two-stage Hf model ages (T_{DM2}) are more reliable to record the extraction timing of source materials from the depleted mantle or the average crustal residence duration of crustal precursors. The investigated felsite zircons show two-stage model ages (T_{DM2}) of 1092–1334 Ma.

Zircons from rhyolite porphyry yield $^{176}Hf/^{177}Hf$ ratios ranging from 0.282670 to 0.282790, with $\varepsilon_{Hf}(t)$ values of −0.65 to +3.58 and a mean value of +1.39. Among all analyzed grains, eleven zircons have positive $\varepsilon_{Hf}(t)$ values and only one exhibits a negative value. Almost all analytical spots cluster near the chondritic evolution line, with merely a single datum plotting below this line (Figure 8a,b). The corresponding two-stage model ages (T_{DM2}) vary between 960 and 1229 Ma (Table S3).

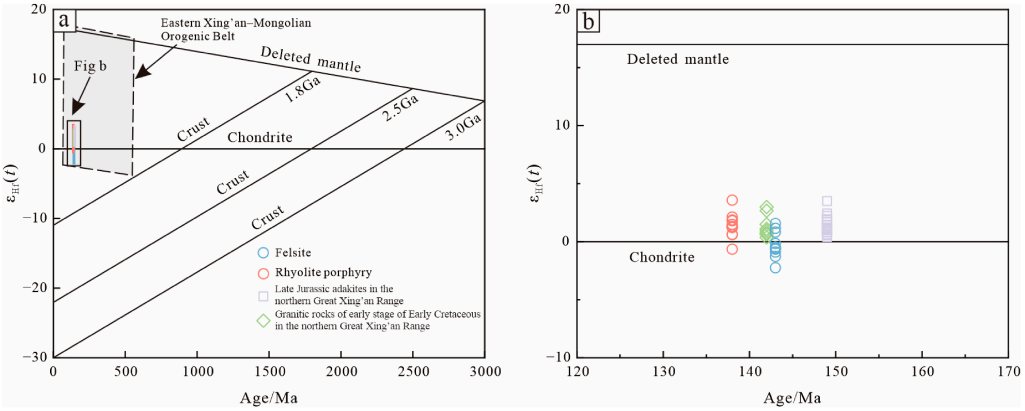


Figure 8. (**a**,**b**) Age-$\varepsilon_{Hf}(t)$ diagrams for zircons of the felsite and the rhyolite porphyry from the Huoluotai area. Data sources are the same as in Figure 6.

5. Discussion

5.1. Petrogenesis and Magmatic Source

5.1.1. Petrogenesis

Numerous classification schemes have been proposed for granites, among which the subdivision into I-, S-, A- and rarely occurring M-type granites is most widely adopted [40,41]. M-type granites generally originate from fractional crystallization of mafic magmas in crustal magma chambers and are characteristic components of ophiolite sequences. This petrogenetic setting is distinctly inconsistent with the field occurrence of the Huoluotai subvolcanic granitic intrusions. Neither the felsite nor the rhyolite porphyry hosts characteristic Al-rich minerals indicative of S-type granites, including garnet, muscovite and cordierite. S-type granites commonly exhibit high P_2O_5 concentrations (>0.20 wt.%), with P_2O_5 progressively accumulating during magmatic differentiation [42]. The felsite and rhyolite porphyry yield P_2O_5 contents of 0.01–0.02 wt.% and 0.03–0.04 wt.%, respectively, all less than 0.10 wt.%, which rules out an S-type affinity for the investigated intrusions.

Their Zr concentrations range from 91.62 ppm to 116.39 ppm for the felsite and 167.65 ppm to 222.58 ppm for the rhyolite porphyry, with (Zr + Nb + Ce + Y) values of 120.81 ppm–155.42 ppm and 279.50 ppm–341.42 ppm, respectively. These geochemical signatures conflict with the diagnostic criteria for A-type granites, which are characterized by abundant alkaline minerals and enrichment of high-field-strength elements including Ga, Zr, Nb and Ta; typical thresholds for A-type granites include Zr > 250 ppm and (Zr + Nb + Ce + Y) > 350 ppm [41,43,44]. Zircon saturation temperature (T_{Zr}, °C) can be used to estimate the temperature of partial melting and melt segregation from the magma source [45]. The calculated T_{Zr} values range from 755 to 768.16 °C (mean = 759.50 °C) for the felsite and 817.69 to 848.52 °C (mean = 834.46 °C) for the rhyolite porphyry. Although the rhyolite porphyry records higher crystallization temperatures, these values are still lower than the formation temperature (845–880 °C) of Late Yanshanian A-type granites in the Tongbai–Dabie orogen [46], consistent with the typical temperature range of I-type granites.

Harker diagram plots show that major oxides (e.g., MgO) and Th contents gradually decrease with increasing SiO_2 in both felsite and rhyolite porphyry (Figure 9), indicating that these rocks were primarily formed via fractional crystallization of cogenetic magmas. The distinct Ba depletion observed in the samples is controlled by K-feldspar fractional crystallization, whereas low CaO/Al_2O_3 ratios, negative Eu anomalies and Sr depletion reflect extensive plagioclase fractionation. In addition, Ti depletion is attributed to the fractionation of Ti-bearing minerals such as rutile and ilmenite, while intense P depletion

is caused by fractional crystallization of apatite during magmatic evolution. The Ga/Al ratios of the studied rocks tend to increase with decreasing Zr contents, recording the evolutionary trend of fractionated I- and S-type granites (Figure 10a), which is distinct from that of A-type granites [47]. The A/CNK ratios display a similar increasing trend with the reduction in Zr contents (Figure 10b), indicative of amphibole fractional crystallization during the evolution of I-type granites [48]. Furthermore, the samples have low P_2O_5 abundances, and SiO_2 shows a pronounced negative correlation with P_2O_5 (Figure 9e), collectively confirming the typical I-type affinity of these rocks [49]. This result is consistent with previous regional studies, which have demonstrated that Mesozoic granites in the northern Great Xing'an Range are predominantly I-type granites [50–52].

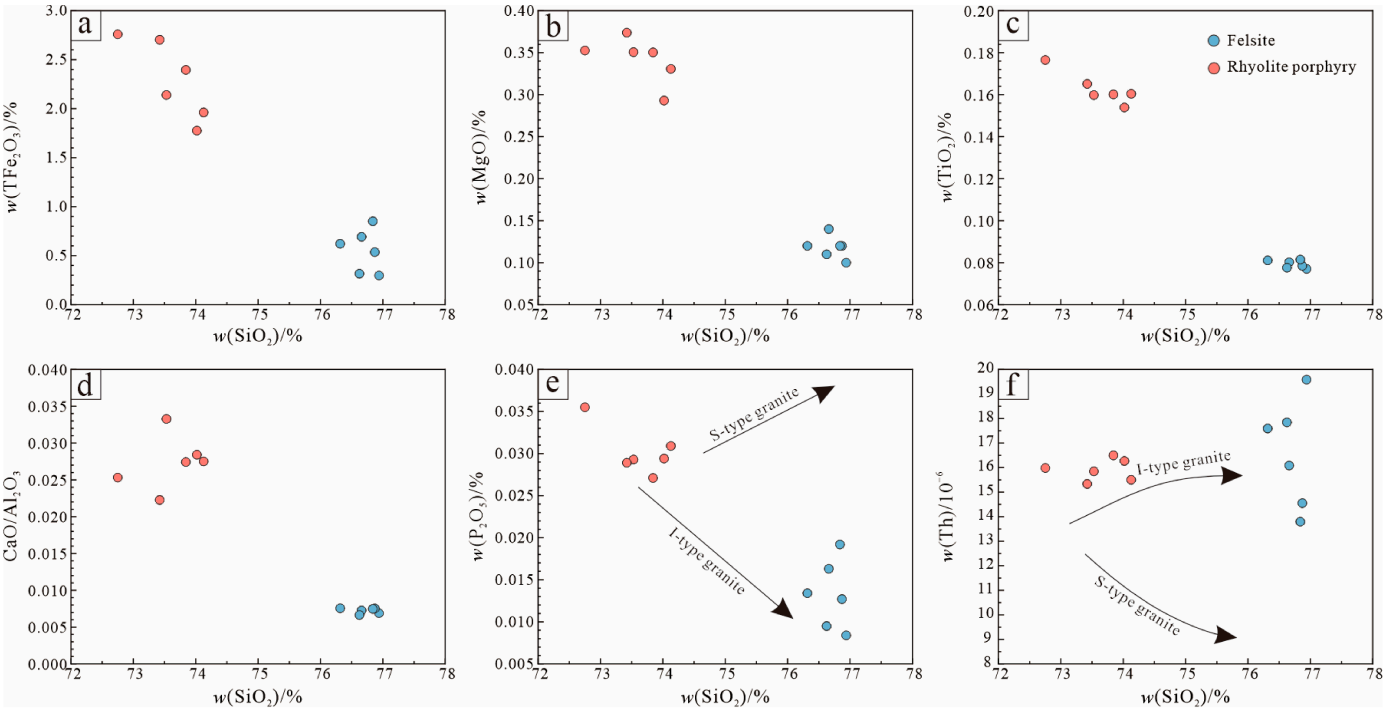


Figure 9. Haker diagrams of the felsite and the rhyolite porphyry from the Huoluotai area. (**a**) TFe_2O_3-SiO_2 diagram; (**b**) MgO-SiO_2 diagram; (**c**) TiO_2-SiO_2 diagram; (**d**) CaO/Al_2O_3-SiO_2 diagram; (**e**) P_2O_5-SiO_2 diagram and (**f**) Th-SiO_2 diagram.

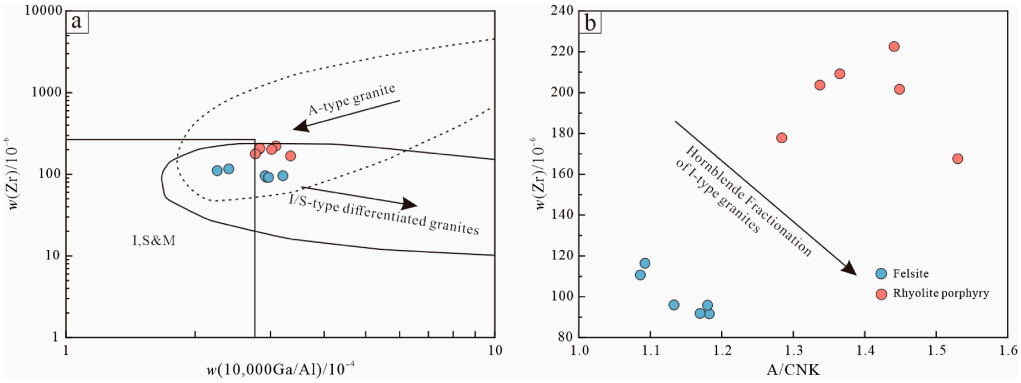


Figure 10. (**a**) Zr-Ga/Al diagram [47] and (**b**) Zr-A/CNK diagram [41] of the felsite and the rhyolite porphyry from the Huoluotai area.

Intense fractional crystallization during the formation of highly fractionated granites results in Nb/Ta and Zr/Hf ratios departing from continental crust averages [53–55]. Empirically, Nb/Ta < 17 and Zr/Hf < 38 are widely used to discriminate highly fractionated

granites [47]. In this study, the analyzed felsite and rhyolite porphyry yield Nb/Ta of 13.8–15.6 and 14.5–15.6, and Zr/Hf of 29.3–32.8 and 32.0–36.1, respectively, all consistent with the characteristics of highly fractionated granites. It should be clarified that these ratio variations are not inherited from the magma source, but are generated by continuous fractional crystallization throughout magma evolution. In addition, Nb contents of the samples show a positive correlation with Ta contents (Figure 11a), while Nb/Ta ratios decrease with increasing Ta contents (Figure 11b). Both Hf contents and Zr/Hf ratios display positive correlations with Zr contents (Figure 12a,b). This regular covariation cannot be produced by random accumulation or localized fractionation of individual accessory mineral grains in the late magmatic stage, which would normally produce scattered and discontinuous data arrays. Instead, it records a sustained, system-wide fractionation process of Ti-bearing oxides (rutile, titanite), amphibole and zircon. The fractionation of Nb-Ta and Zr-Hf bearing minerals is an integral part of the overall magmatic differentiation process, rather than an isolated late-stage event.

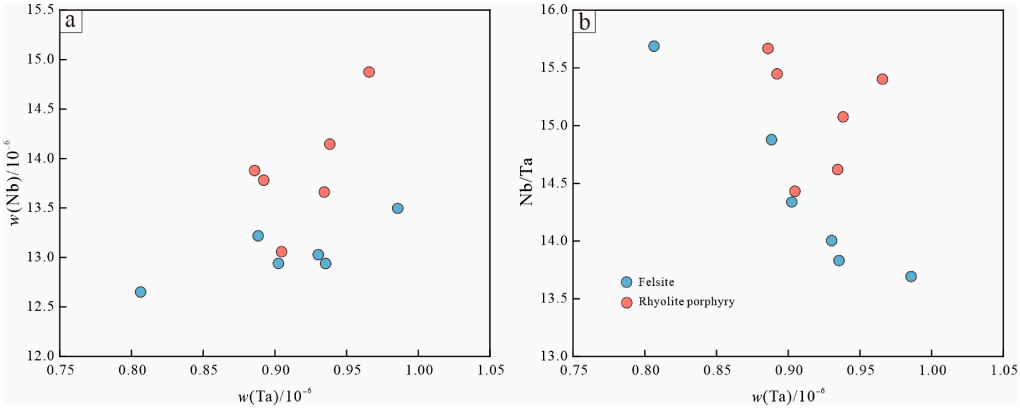


Figure 11. (**a**) Nb-Ta diagram and (**b**) Nb/Ta-Ta diagram of the felsite and the rhyolite porphyry from the Huoluotai area.

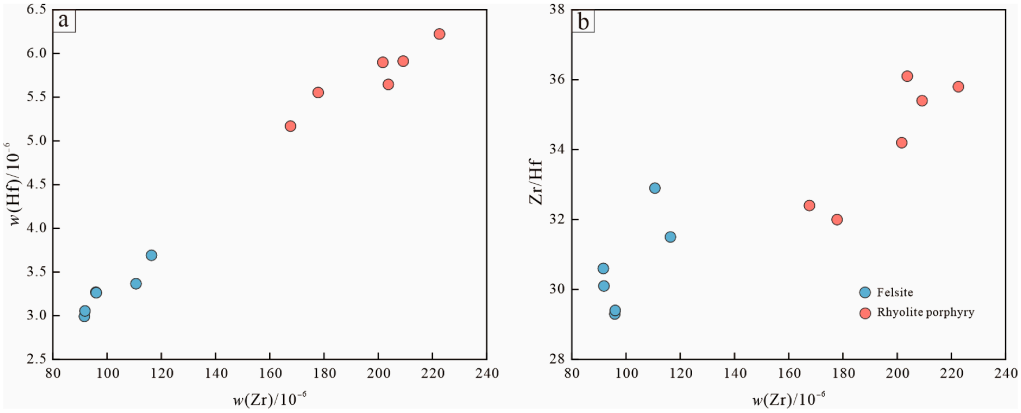


Figure 12. (**a**) Hf-Zr diagram and (**b**) Zr/Hf-Zr diagram of the felsite and the rhyolite porphyry from the Huoluotai area.

However, we acknowledge that whole-rock geochemical data alone cannot fully constrain the exact fractional crystallization pathway, nor can they provide definitive evidence for the continuous control of these specific mineral phases over the entire differentiation sequence. The Nb/Ta and Zr/Hf ratios presented here are therefore interpreted primarily as proxies for the degree of magmatic fractionation, and the inferred mineral fractionation mechanisms should be regarded as tentative. Further mineralogical evidence or quantitative fractional crystallization modeling would be required to verify the detailed

fractionation processes and mineral controls. Accordingly, the low Nb/Ta and Zr/Hf ratios, combined with their systematic covariation trends, provide robust evidence for the highly fractionated nature of the studied intrusions. These geochemical variations are consistent with those of highly fractionated granites from the Fogang pluton in Guangdong Province [56], further demonstrating that both the felsite and rhyolite porphyry belong to highly fractionated granites.

5.1.2. Magmatic Source

In general, two dominant mechanisms are widely accepted to interpret granite genesis: (1) partial melting of crustal rocks [57–59]; and (2) extensive fractional crystallization of mantle-derived intermediate–mafic parent magmas [60]. Early Cretaceous granitoids are widely exposed in the study area, so they are unlikely to be derived from differentiation of intermediate-mafic magmas. The rocks are enriched in large ion lithophile elements (e.g., Rb, K, Th, U) and depleted in high-field-strength elements (e.g., P, Ta, Nb, Ti), showing close geochemical affinity to average continental crust compositions [61–63]. Felsite and rhyolite porphyry yield La/Sm ratios of 11.4–11.7 and 9.3–16.1, respectively, consistent with typical continental crust values (<15) [37]. Their Ce/Pb ratios range from 0.1–0.4 and 0.1–2.2, falling within the continental crust range (<3.9) [64] (pp. 1–51). The Ti/Y ratios are 81.7–87.8 (avg. = 85.3) for felsite and 96.2–131.5 (avg. = 111.3) for rhyolite porphyry, both below the upper continental crust threshold of 200 [64] (pp. 1–51). In addition, Ti/Zr ratios vary from 4.6–5.9 (avg. = 5.0) and 4.0–5.3 (avg. = 4.8), respectively, well within the continental crust range (<30) [64] (pp. 1–51). Mantle-derived magmas generally have significantly higher Ti/Zr and Ti/Y ratios than continental crust, and these ratios indicate that the felsite and rhyolite porphyry are neither directly derived from mantle partial melting nor evolved from mantle-derived magmas by fractional crystallization, favoring a crustal origin for their parent magmas [65]. This interpretation is corroborated by the low $Mg^{\#}$ values of the samples (24.05–45.64 for felsite and 22.94–28.20 for rhyolite porphyry), which are characteristic of crustal sources (crustal-derived $Mg^{\#}$ = 10–40 and mantle-derived $Mg^{\#} \approx 70$) [66]. Given that $Mg^{\#}$ is highly sensitive to input of mantle-derived mafic components, the low $Mg^{\#}$ values of our samples indicate no significant involvement of high-$Mg^{\#}$ mantle components during magma formation [67].

Previous studies on Hf isotopes of magmatic zircons indicate that magmatic rocks with positive zircon $\varepsilon_{Hf}(t)$ values are generally derived either directly from the mantle or from partial melting of juvenile crust generated by differentiation of mantle-derived materials, whereas those with negative zircon $\varepsilon_{Hf}(t)$ values generally originate from an ancient crust or form after significant crustal contamination [38]. Zircon $\varepsilon_{Hf}(t)$ values of felsite and rhyolite porphyry range from −2.25 to +1.57 and −0.65 to +3.58, respectively. All analytical data cluster near the chondritic evolution line and show features of slight depletion coupled with weak enrichment (Figure 8a,b). Combined with the above constraint of a crust-derived magma source, the felsite yields moderately positive to weakly negative $\varepsilon_{Hf}(t)$ values and two-stage Hf model ages (T_{DM2}) of 1092–1344 Ma, suggesting that its magma source was most likely derived from partial melting of Mesoproterozoic juvenile basaltic crust with minor ancient silicic crustal components. By contrast, nearly all rhyolite porphyry zircons have positive $\varepsilon_{Hf}(t)$ values and T_{DM2} of 960–1229 Ma, indicating a source dominated by Mesoproterozoic juvenile basaltic crust, with limited contributions from silicic crust. Both the felsite and rhyolite porphyry in this study yield $\varepsilon_{Hf}(t)$ values consistent with the published data of Phanerozoic igneous rocks from the Great Xing'an Range [68], indicating that crustal accretion events occurred in the Great Xing'an Range during the Late Precambrian [69].

5.2. Tectonic Setting of Granitic Intrusions and Implications for the Regional Tectonic Transition

Located at the intersection of the Mongol–Okhotsk and Paleo-Pacific tectonic domains, the northern Great Xing'an Range has long been the subject of debate regarding its Mesozoic magmatic and tectonic evolution. Late Jurassic to earliest Early Cretaceous igneous rocks in Northeast China are primarily distributed west of the Songliao Basin, forming a broad NE-trending magmatic belt. This belt extends westward into Transbaikalia and central–eastern Mongolia, parallel to the strike of the Mongol–Okhotsk suture zone, and exhibits a distinct west-to-east younging trend of volcanic rock ages [70,71]. In contrast, coeval magmatism is generally absent in eastern Jilin–Heilongjiang provinces east of the Songliao Basin [3,72,73], with only two Late Jurassic (~147 Ma) felsic dykes documented in the Zhangguangcai Range [7]. Moreover, large-scale extensional magmatism driven by Paleo-Pacific slab rollback did not commence in eastern northeastern China until ~130 Ma [3], which is significantly later than the 143.4–138.8 Ma extensional intrusions reported in this study. Geochemically, the studied rocks show typical features of intracrustal reworking, with no obvious subduction fluid imprint characteristic of a Paleo-Pacific arc setting. Collectively, multiple lines of evidence support that the late Jurassic–earliest Early Cretaceous magmatism in the northern Great Xing'an Range was most likely dominated by the tectonic evolution of the eastern Mongol–Okhotsk system. However, given the superimposed tectonic setting of the study area, a potential remote superimposed influence of the Paleo-Pacific tectonic regime cannot be completely ruled out based on the current geochemical and geochronological dataset. Further systematic isotopic and structural investigations are required to quantify the respective contributions of the two tectonic domains.

Genetic deposit types can directly and precisely constrain metallogenic tectonic settings. For instance, two major porphyry Mo metallogenic belts with significant exploration breakthroughs have been identified in Northeast China since the beginning of this century: one in the eastern Jilin–Heilongjiang region and the other in the northern Great Xing'an Range. Both belts host subduction-related porphyry Mo deposits, but they show clear differences in mineralization timing. Porphyry Mo mineralization in the eastern Jilin–Heilongjiang belt formed mainly during the Early–Middle Jurassic, with a prominent peak in the Middle Jurassic [3,58,74,75], whereas the Mo mineralization event in the northern Great Xing'an Range is tightly constrained to the Late Jurassic [17,36,76]. These distinct spatiotemporal patterns demonstrate that the two episodes of porphyry Mo mineralization during the Early Yanshanian were controlled by two independent oceanic subduction tectonic systems.

Previous studies have discussed that the evolutionary process of the eastern Mongol–Okhotsk Ocean remains poorly constrained. The distinct geochemical variations of granites across the Jurassic–Cretaceous boundary in the northern Great Xing'an Range provide critical evidence for constraining the timing of tectonic regime transition in the eastern Mongol–Okhotsk Ocean. Late Jurassic ore-related granitoids and associated porphyry Mo deposits in the northern Great Xing'an Range are concentrated at 150–146 Ma (Table 1). Their ore-bearing porphyries (granodiorite porphyry and monzogranite porphyry) belong to calc-alkaline to high-K calc-alkaline and metaluminous to weakly peraluminous series (Figure 6c,d). These rocks are characterized by high Na_2O and low K_2O contents with K_2O/Na_2O ratios less than 1, as well as high Sr/Y ratios and low Y and Yb concentrations, showing geochemical signatures of O-type adakites [17,34,77]. Such geochemical features indicate that the magmas were generated by partial melting of the subducted oceanic slab [17,34]. Earliest Early Cretaceous igneous rocks are widely exposed in the northern Great Xing'an Range (Table 2). The felsite (143.4 ± 1.2 Ma) and rhyolite porphyry (138.8 ± 2.0 Ma) from the Holuotai area are important constituents of this extensional

magmatic event. These rocks are characterized by remarkably high K_2O and low Na_2O contents with $K_2O/Na_2O > 1$. They belong to weakly peraluminous to peraluminous and high-K calc-alkaline to shoshonitic series, and exhibit low Sr and Yb concentrations. Such geochemical signatures are consistent with those of coeval Early Cretaceous granitoids in the northern Great Xing'an Range (Figure 6c,d), but distinctly differ from the Late Jurassic Na-rich adakites derived from partial melting of subducted oceanic slab.

Table 1. Geochronological data of ore-forming intrusions and mineralization for Late Jurassic porphyry molybdenum deposits in the northern Great Xing'an Range.

No.	Sample ID	Locality	Analyzed Material	Age (Ma)		Data Source
1	XKL-N1	Xiaokelehe	granodiorite porphyry	zircon U–Pb	148.8 ± 1.1 Ma	[17]
2		Xiaokelehe	ore	molybdenite Re–Os	148.7 ± 0.9 Ma	[17]
3	HLT-ZK18-2-TW1	Huoluotai	granodiorite porphyry	zircon U–Pb	148.9 ± 0.9 Ma	[17]
4		Huoluotai	ore	molybdenite Re–Os	146.8 ± 0.9 Ma	[17]
5		Fukeshan	quartz diorite porphyry	zircon U–Pb	148.7 ± 0.8 Ma	[34]
6	1702-289	Chalukou	granite porphyry	zircon U–Pb	147 ± 1 Ma	[77]
7		Chalukou	ore	molybdenite Re–Os	146.9 ± 0.8 Ma	[78]

Table 2. Zircon U–Pb ages of early Early Cretaceous magmatic rocks in the northern Great Xing'an Range.

No.	Sample ID	Locality	Latitude	Longitude	Analyzed Material	Age (Ma)	Data Source
1	GFK21	Fukeshan			andesite	145 ± 1	[34]
2	806-222	Chalukou			diorite porphyrite	142 ± 3	[77]
3	GW03285	Mangui	52°03′27″ N	122°05′33″ E	diabase	133 ± 3	[15]
4	D0014	Tahe	52°33′54″ N	124°33′39″ E	basaltic andesite	136.0 ± 1.2	[74]
5	JLG-01	Jielugonghe	51°53′46.4″ N	121°00′06.9″ E	basaltic andesite	138.8 ± 1.1	[79]
6	JGD-05	Woduhe	50°33′53″ N	125°41′47″ E	granite	136 ± 1	[79]
7	1558-3	Xinlin	51°35′30″ N	120°16′25″ E	quartz monzonite	135 ± 3	[80]
8	1561-2	Xinlin	51°35′30″ N	120°16′25″ E	quartz monzonite	141 ± 2	[80]
9	1562-1	Xinlin	51°37′42.5″ N	124°22′59.6″ E	quartz monzonite	141.1 ± 1.7	[80]
10	HLT-TC16-3N7	Huoluotai			diorite	140 ± 1	[81]
11	PM015TC38	Zhanbeicun	51°57′06″ N	124°24′05″ E	rhyolite	136.9 ± 1.3	[82]
12	B3050	Kaikukang	53°06′36″ N	124°14′13″ E	rhyolitic tuff	136.6 ± 1.9	[83]
13	B1166	Kaikukang	53°06′36″ N	124°45′04″ E	rhyolitic tuff	137.5 ± 2.5	[83]
14	Pm41D237	Tahe			monzogranite	138 ± 1	[84]
15	Pm47D005	Tahe	53°06′21″ N	125°09′36″ E	monzogranite	138 ± 3	[84]
16	Pm42D126	Tahe	53°03′51″ N	125°17′57″ E	granodiorite	135 ± 4	[84]
17	Pm47D57	Tahe	53°01′40″ N	125°13′53″ E	granodiorite porphyry	137 ± 5	[84]
18	HLT-L9	Huoluotai	52°34′36″ N	122°06′10″ E	felsite	143.4 ± 1.2	This study
19	ZK30-1	Huoluotai	52°30′26″ N	122°50′43″ E	rhyolite porphyry	138.8 ± 2.0	This study

On the Rb-(Y + Nb) and Rb-(Yb + Ta) tectonic discrimination diagrams (Figure 13), all felsite and rhyolite porphyry samples fall into the post-collision domain, which is clearly distinct from Late Jurassic subduction-related granitoids. Multiple recent studies have documented widespread early Early Cretaceous (136–141 Ma) A-type granites across the northern Great Xing'an Range [72], and the coexistence of A- and I-type granites collectively records a typical extensional regime. The Holuotai felsite (143.4 ± 1.2 Ma) and rhyolite porphyry (138.8 ± 2.0 Ma) formed during post-collisional extension, whereas subduction-related porphyry Mo mineralization predominantly occurred at 150–146 Ma. The geochemical transition from Late Jurassic subduction-related adakitic magmatism to Early Cretaceous extensional highly fractionated granitic magmatism, combined with the termination of porphyry Mo mineralization at ca. 146 Ma, constrains the tectonic regime

transition from compression to extension in the northern Great Xing'an Range at ~145 Ma. It should be noted that this timing represents the local tectonic transition in the easternmost segment of the orogenic belt, rather than the definitive final closure age of the entire eastern Mongol–Okhotsk Ocean. Although the most likely geodynamic trigger for this transition is the final closure of the eastern segment of the Mongol–Okhotsk Ocean, this interpretation requires further direct evidence from the suture zone to confirm. From the perspective of applied geology, the earliest Early Cretaceous post-collisional extensional setting in the northern Great Xing'an Range was accompanied by widespread subvolcanic intrusions and dyke emplacement along extensional faults, which provides favorable conditions for the migration and enrichment of ore-forming fluids. A number of typical deposits formed in the same period and tectonic setting have been identified in the region, including the Biliagu lead–zinc–silver deposit (133.4 Ma) [85], the Chaobuleng Fe-Cu polymetallic deposit (140.7 Ma) [86] and the Shabaosi gold deposit (~130 Ma) [87]. This interval therefore has good prospecting potential for epithermal, porphyry and vein-type polymetallic deposits, and deserves further attention in future regional mineral exploration work.

The Mohe Basin in northern Heilongjiang clearly records the tectonic regime transition of the Mongol–Okhotsk orogenic system. At the end of the Late Jurassic, collisional compressional thrust structures and molasse sequences were developed, which record orogenic uplift and crustal thickening following the closure of the Mongol–Okhotsk Ocean [88,89]. In the earliest Early Cretaceous, the region rapidly shifted to an extensional rift-dominated setting [90,91]. The basin is unconformably overlain by volcanic–sedimentary successions, and voluminous magmatism erupted immediately after the compressional episode. Widespread Early Cretaceous A_2-type granites and rhyolites occur within the study area, which were generated in a tectonic setting of gravitational collapse and thinning of the previously thickened orogenic crust [92]. Collectively, these geological archives document a complete dynamic transition from orogenic uplift to post-orogenic gravitational collapse and extension. Earliest Early Cretaceous magmatism in the northern Great Xing'an Range was likely triggered by gravitational collapse of the thickened orogen after oceanic closure. Within this regional extensional framework, asthenospheric upwelling and mantle-derived magmatic underplating provided heat to the collision-thickened crust and induced crustal partial melting, generating highly fractionated I-type granites. It should be emphasized that these deep crust–mantle processes are interpretive inferences based on regional geological context, and cannot be independently verified by the current dataset. The geochemical transition from adakitic Sr–Ba enrichment to post-collisional Sr–Ba depletion marks the tectonic shift from oceanic subduction to orogenic collapse and post-collisional extension at ~145 Ma. The temporal variation from the highly fractionated felsite (143.4 Ma) to the rhyolite porphyry (138.8 Ma) with more positive zircon $\varepsilon_{Hf}(t)$ values records progressively enhanced crustal extension and increasing asthenospheric mantle input. As extensional intensity increased, mantle-derived magma underplating became more prominent, leading to increased melting in the juvenile lower crust and a greater mantle contribution to the magmatic system.

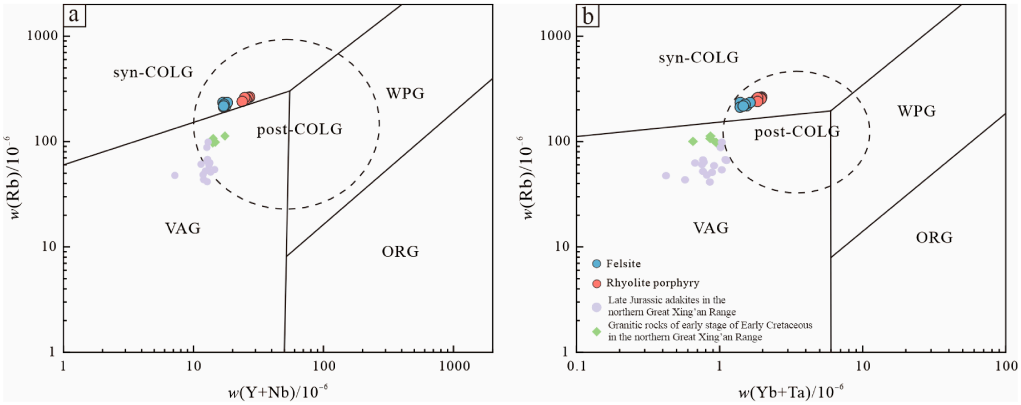


Figure 13. (**a**) Rb-(Y + Nb) and (**b**) Rb-(Yb + Ta) tectonic setting discrimination diagrams [93] of the felsite and the rhyolite porphyry from the Huoluotai area. ORG: mid-ocean ridge granite; VAG: volcanic arc granite; WPG: intraplate granite; Post-COLG: post-collision granite; Syn-COLG: syncollision granite. Data sources are the same as in Figure 6.

Late Early Cretaceous (133–106 Ma) igneous rocks are widely developed across Northeast China with prominent compositional variations among different regions. A suite of calc-alkaline volcanic assemblages was formed in eastern Jilin–Heilongjiang area, recording subduction of the Paleo-Pacific Plate [17,72]. By contrast, bimodal volcanic assemblages predominate in the Songliao Basin and Great Xing'an Range [94,95], which likely formed in a back-arc extensional setting related to subduction of the Paleo-Pacific Plate beneath the Eurasian Continent [72]. Such Spatial variations in volcanic rock assemblages from the Northeast Asian continental margin toward the intracontinental domain record the occurrence of Paleo-Pacific Plate subduction [3,72]. Collectively, the late Early Cretaceous igneous rocks in Northeast China were probably predominantly formed in response to subduction of the Paleo-Pacific Plate beneath the Eurasian continent, and the widely exposed coeval high-Mg adakites [8] are genetically linked to lithospheric delamination.

Integrating the geochronological, geochemical and zircon Hf isotopic data from this study with regional geological records, we document a tectonic regime transition from compression to extension at ~145 Ma in the northern Great Xing'an Range. This transition is directly recorded by the geochemical shift from Late Jurassic subduction-related adakitic magmatism to earliest Early Cretaceous extensional highly fractionated granitic magmatism, as well as the termination of subduction-related porphyry Mo mineralization. In summary, a three-stage tectonic evolutionary model is established for the Late Jurassic–earliest Early Cretaceous transition in the northern Great Xing'an Range (Figure 14): (1) During the Late Jurassic (~150–146 Ma), southward subduction of the Mongol–Okhotsk oceanic slab produced widespread adakitic arc magmatism and porphyry Mo mineralization under a compressional setting (Figure 14a). (2) At the Jurassic–Cretaceous boundary (~145 Ma), the tectonic regime shifts from compression to extension (Figure 14b). (3) During the earliest Early Cretaceous (144–133 Ma), extensive partial melting of the Mesoproterozoic juvenile lower crust occurred under the post-collisional extensional setting, and the resultant magmas underwent strong fractional crystallization during ascent along extensional faults, finally forming the highly fractionated felsite and rhyolite porphyry intrusions in the Huoluotai area (Figure 14c).

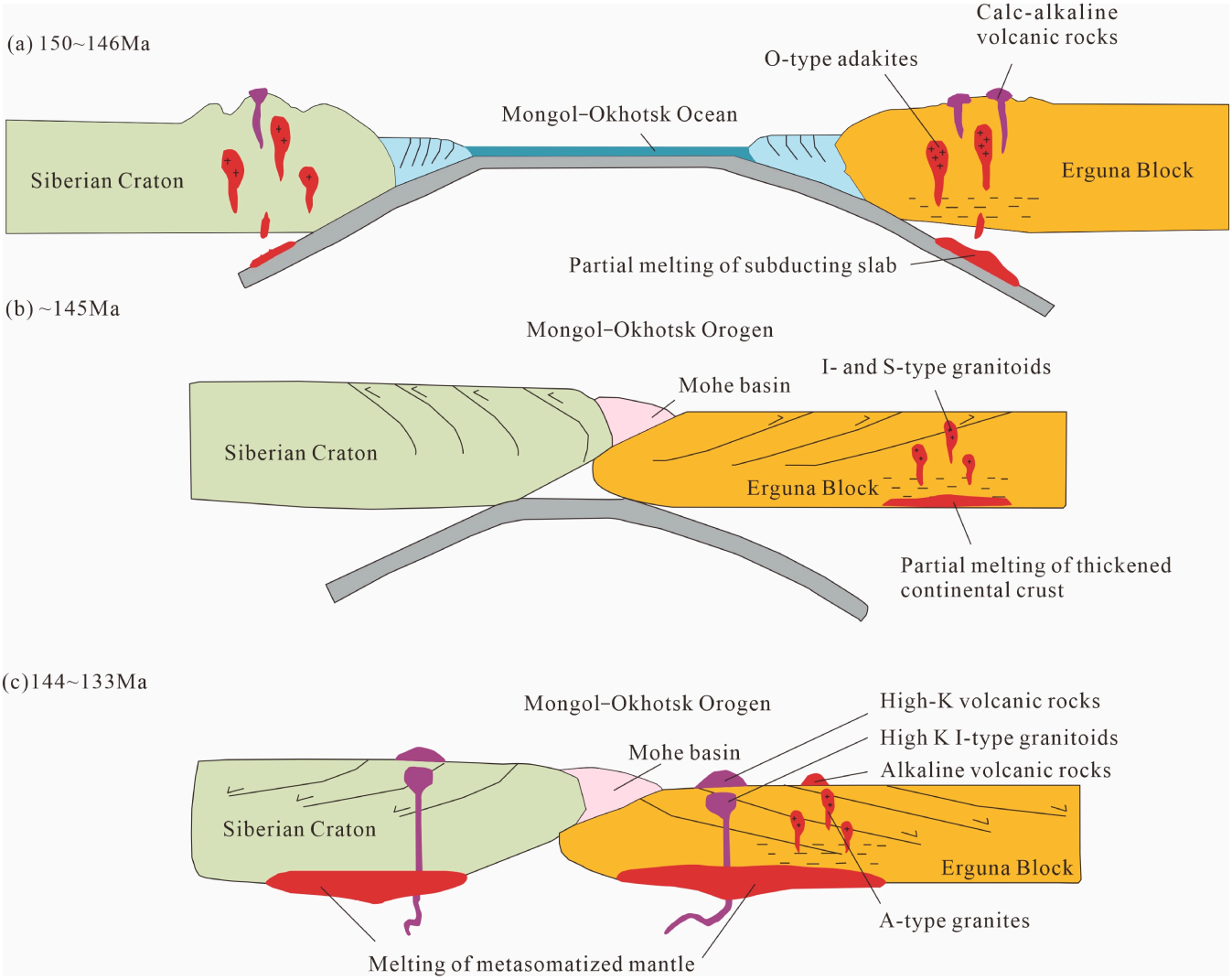


Figure 14. Tectonic evolution model of the Mongol–Okhotsk Ocean during the Late Jurassic to earliest Early Cretaceous showing subduction (**a**), tectonic transition (**b**), and extensional (**c**) stages [96]. Note that deep crust–mantle processes (gravitational collapse, asthenospheric upwelling and mantle underplating) are speculative interpretations based on regional geological context, while shallow magmatic features and timing are directly constrained by geochronological and geochemical data.

6. Conclusions

(1) The Holuotai felsite and rhyolite porphyry yield zircon U–Pb crystallization ages of 143.4 ± 1.2 Ma and 138.8 ± 2.0 Ma, respectively. They belong to K-rich highly fractionated I-type granites and are characterized by low Sr and Yb contents. Their parent magmas were predominantly derived from Mesoproterozoic juvenile crust, with variable degrees of contamination by ancient silicic crustal materials.

(2) These felsic magmatic rocks formed in a post-collisional extensional environment, constraining the final closure of the eastern Mongol–Okhotsk Ocean to earlier than ~144 Ma.

(3) Subduction-related porphyry Mo mineralization in the northern Great Xing'an Range mainly occurred at 150–146 Ma, representing a compressional tectonic stage. The earliest Early Cretaceous therefore records a crucial tectonic transition at ~145 Ma in the eastern Mongol–Okhotsk domain, marking a shift from regional compression to post-collisional extension.

Supplementary Materials: The following supporting information can be downloaded at: https://www.mdpi.com/article/10.3390/min16090899/s1, Table S1: Zircon U–Pb geochronological results of felsite and rhyolite porphyry from the Huoluotai area; Table S2: Major (wt.%), rare earth and trace elements ($\times 10^{-6}$) content and parameter of the felsite and the rhyolite porphyry from the Huoluotai area and Table S3: Zircon Lu–Hf isotopic compositions of the felsite and the rhyolite porphyry from the Huoluotai area.

Author Contributions: Conceptualization, G.L. and B.L.; methodology, G.L. and B.L.; software, Z.L., L.Z. and G.L.; validation, G.L. and B.L.; formal analysis, G.L., B.L., L.Z. and X.L.; investigation, G.L., B.L., Z.L., L.Z. and X.L.; resources, Z.L., X.L. and B.L.; data curation, G.L., L.Z. and B.L.; writing—original draft preparation, G.L. and B.L.; writing—review and editing, G.L., Z.L., L.Z. and B.L.; visualization, G.L.; supervision, Z.L. and B.L.; project administration, Z.L., B.L. and X.L.; funding acquisition, Z.L., B.L. and X.L. All authors have read and agreed to the published version of the manuscript.

Funding: This research was funded by the Deep Resources Exploration and Mining Special Project of the National Key R&D Program of China (SQ2025AAA060086).

Data Availability Statement: All data is contained within the article or Supplementary Materials.

Acknowledgments: The authors thank B.L and the teachers for their contributions, which have improved this paper and assisted in its completion. The authors thank the editor and anonymous reviewers for their helpful and constructive comments, which have greatly improved the quality of this paper.

Conflicts of Interest: Author Gantian Li was employed by the company Zhongze Holding Group Co., Ltd. The remaining authors declare that the research was conducted in the absence of any commercial or financial relationships that could be construed as a potential conflict of interest.

References

1. Jahn, B.M.; Wu, F.Y.; Chen, B. Granitoids of the Central Asian Orogenic Belt and continental growth in the Phanerozoic. *Earth Environ. Sci. Trans. R. Soc. Edinb.* **2000**, *91*, 181–193. [CrossRef]
2. Windley, B.F.; Alexeiev, D.; Xiao, W.J.; Kroner, A.; Badarch, G. Tectonic models for accretion of the Central Asian Orogenic Belt. *J. Geol. Soc.* **2007**, *164*, 31–47. [CrossRef]
3. Xu, W.L.; Pei, F.P.; Wang, F.; Meng, E.; Ji, W.Q.; Yang, D.B.; Wang, W. Spatial–temporal relationships of Mesozoic volcanic rocks in NE China: Constraints on tectonic overprinting and transformations between multiple tectonic regimes. *J. Asian Earth Sci.* **2013**, *74*, 167–193. [CrossRef]
4. Xu, W.L.; Sun, C.Y.; Tang, J.; Luan, J.P.; Wang, F. Basement nature and tectonic evolution of the Xing'an–Mongolian Orogenic belt. *Earth Sci.* **2019**, *44*, 1620–1646. (In Chinese) [CrossRef]
5. Zhou, J.B.; Wilde, S.A.; Zhao, G.C.; Han, J. Nature and assembly of microcontinental blocks within the Paleo-Asian Ocean. *Earth-Sci. Rev.* **2018**, *186*, 76–93. [CrossRef]
6. Liu, Y.J.; Li, W.M.; Feng, Z.Q.; Wen, Q.B.; Neubauer, F.; Liang, C.Y. A review of the Paleozoic tectonics in the eastern part of Central Asian Orogenic Belt. *Gondwana Res.* **2017**, *43*, 123–148. [CrossRef]
7. Wu, F.Y.; Sun, D.Y.; Ge, W.C.; Zhang, Y.B.; Grant, M.L.; Wilde, S.A.; Jahn, B.M. Geochronology of the Phanerozoic granitoids in northeastern China. *J. Asian Earth Sci.* **2011**, *41*, 1–30. [CrossRef]
8. Ji, Z.; Meng, Q.A.; Wan, C.B.; Ge, W.C.; Yang, H.; Zhang, Y.L.; Dong, Y.; Jin, X. Early Cretaceous adakitic lavas and A-type rhyolites in the Songliao Basin, NE China: Implications for the mechanism of lithospheric extension. *Gondwana Res.* **2019**, *71*, 28–48. [CrossRef]
9. Zorin, Y.A. Geodynamics of the western part of the Mongolia-Okhotsk collisional belt, Trans-Baikal region (Russia) and Mongolia. *Tectonophysics* **1999**, *306*, 33–56. [CrossRef]
10. Metelkin, D.V.; Vernikovsky, V.A.; Kazansky, A.Y. Late Mesozoic tectonics of Central Asia based on paleomagnetic evidence. *Gondwana Res.* **2010**, *18*, 400–419. [CrossRef]
11. Yang, Y.T.; Song, C.C.; He, S. Jurassic tectonostratigraphic evolution of the Junggar basin, NW China: A record of Mesozoic intraplate deformation in Central Asia. *Tectonics* **2015**, *34*, 86–115. [CrossRef]
12. Guo, Z.X.; Yang, Y.T.; Zyabrev, S.V.; Hou, Z.H. Tectonostratigraphic evolution of the Mohe-Upper Amur Basin reflects the final closure of the Mongol-Okhotsk Ocean in the latest Jurassic–earliest Cretaceous. *J. Asian Earth Sci.* **2017**, *145*, 494–511. [CrossRef]

13. Wu, L.; Kravchinsky, V.A.; Gu, Y.J.; Potter, D.K. Absolute reconstruction of the closing of the Mongol-Okhotsk Ocean in the Mesozoic elucidates the genesis of the slab geometry underneath Eurasia. *J. Geophys. Res. Solid Earth* **2017**, *122*, 4831–4851. [CrossRef]
14. Zhang, K.J.; Yan, L.L.; Ji, C. Switch of NE Asia from extension to contraction at the mid_Cretaceous: A tale of the Okhotsk oceanic plateau from initiation by the Perm Anomaly to extrusion in the Mongol–Okhotsk ocean? *Earth-Sci. Rev.* **2019**, *198*, 102941. [CrossRef]
15. Zhang, J.H.; Ge, W.C.; Wu, F.Y.; Wilde, S.A.; Yang, J.H.; Liu, X.M. Large-scale Early Cretaceous volcanic events in the northern Great Xing'an Range, Northeastern China. *Lithos* **2008**, *102*, 138–157. [CrossRef]
16. Jing, Y.; Zhang, Y.L.; Wang, Q.H.; Liu, X.W.; Chen, H.J. Petrogenesis of Early Cretaceous miarolitic monzogranite in Longjiang region of northern Great Xing'an Range and its tectonic implications. *Glob. Geol.* **2019**, *38*, 655–667. (In Chinese) [CrossRef]
17. Sun, Y.G. Study on Metallogenesis and Prospecting Direction of Late Jurassic Porphyry Cu (Mo) Deposits in the Northern Segment of the Great Xing'an Range. Ph.D. Thesis, Jilin University, Changchun, China, 2021. (In Chinese)
18. Shao, J.A.; Zhang, L.Q.; Jia, W.; Wang, P.Y. Harkin metamorphic core complex in Inner Mongolia and its upwelling mechanism. *Acta Petrol. Sin.* **2001**, *17*, 283–290. (In Chinese)
19. Abdel-Karim, A. Petrological and Geochemical Characteristics of Miocene-Pleistocene Basaltic Alkaline Subvolcanics of Gharyan District, NW Libya. *J. Earth Sci. Res.* **2014**, *2*, 137–147. [CrossRef]
20. Gong, X.; Zhao, Y.Y.; Shui, X.F.; Cheng, X.D.; Wang, Y.C.; Liu, X.; Tan, W. Zircon U-Pb chronology, Hf isotope and geochemistry studies of the Early Cretaceous rock mass in the Hulalin of Upper Heilongjiang basin. *Acta Geol. Sin.* **2020**, *94*, 553–572. (In Chinese)
21. Meng, F.B. Petrogenesis of diorite porphyrite in Huoluotai area of northern Great Xing'an Range. *J. Heilongjiang Univ. Sci. Technol.* **2022**, *32*, 13–19, 26. (In Chinese)
22. Cui, Y.B.; Wang, K.; He, F.B.; Yin, G.W.; Wang, Z.L.; Wang, G.L.; She, S.K. Geochronology and geochemical characteristics of volcanic rocks from the Manitu Formation in the Qilibin area, northern Great Xing'an Range and its geological significance. *Acta Geol. Sin.* **2021**, *95*, 3301–3316. (In Chinese)
23. Sun, C.Y.; Tang, J.; Xu, W.L.; Li, Y.; Zhao, S. Crustal accretion and reworking processes of micro-continental massifs within orogenic belt: A case study of the Erguna Massif, NE China. *Sci. China Earth Sci.* **2017**, *60*, 1256–1267. [CrossRef]
24. Sun, Y.G.; Li, B.L.; Xie, S.X.; Jin, H.Y.; Ling, S.W.; Li, H.J. Zircon U–Pb dating, petrogeochemical characteristics and tectonic setting of diabase in Huoluotai area, northern segment of Erguna Block. *World Geol.* **2025**, *44*, 22–34. (In Chinese)
25. Wu, F.Y.; Yang, Y.H.; Xie, L.W.; Yang, J.H.; Xu, P. Hf isotopic compositions of the standard zircons and baddeleyites used in U–Pb geochronology. *Chem. Geol.* **2006**, *234*, 105–126. [CrossRef]
26. Griffin, W.L.; Pearson, N.J.; Belousova, E.; Jackson, S.E.; Achterbergh, E.V.; O'Reilly, S.Y.; Shee, S.R. The Hf isotope composition of cratonic mantle: LAM-MC-ICPMS analysis of zircon megacrysts in kimberlites. *Geochim. Cosmochim. Acta* **2000**, *64*, 133–147. [CrossRef]
27. Griffin, W.L.; Wang, X.; Jackson, S.E.; Pearson, N.J.; O'Reilly, S.Y.; Xu, X.; Zhou, X. Zircon chemistry and magma mixing, SE China: In-situ analysis of Hf isotopes, Tonglu and Pingtan igneous complexes. *Lithos* **2002**, *61*, 237–269. [CrossRef]
28. Griffin, W.L.; Belousova, E.A.; Shee, S.R.; Pearson, N.J.; O'Reilly, S.Y. Archean crustal evolution in the northern Yilgarn Craton: U–Pb and Hf-isotope evidence from detrital zircons. *Precambrian Res.* **2004**, *131*, 231–282. [CrossRef]
29. Wu, Y.B.; Zheng, Y.F. Mineralogical study of zircon genesis and its constraints on U-Pb age interpretation. *Chin. Sci. Bull.* **2004**, *49*, 1589–1604. (In Chinese) [CrossRef]
30. Middlemost, E.A.K. Naming materials in the magma/igneous rock system. *Earth-Sci. Rev.* **1994**, *37*, 215–224. [CrossRef]
31. Maniar, P.D.; Piccoli, P.M. Tectonic discrimination of granitoids. *Geol. Soc. Am. Bull.* **1989**, *101*, 635–643. [CrossRef]
32. Peccerillo, A.; Taylor, S.R. Geochemistry of eocene calc-alkaline volcanic rocks from the Kastamonu area, Northern Turkey. *Contrib. Miner. Petrol.* **1976**, *58*, 63–81. [CrossRef]
33. Deng, C.Z.; Sun, D.Y.; Han, J.S.; Li, G.H.; Feng, Y.Z.; Xiao, B.; Li, R.C.; Shi, H.L.; Xu, G.Z.; Yang, D.G. Ages and petrogenesis of the Late Mesozoic igneous rocks associated with the Xiaokele porphyry Cu–Mo deposit, NE China and their geodynamic implications. *Ore Geol. Rev.* **2019**, *107*, 417–433. [CrossRef]
34. Deng, C.Z.; Sun, D.Y.; Han, J.S.; Chen, H.Y.; Li, G.H.; Xiao, B.; Li, R.C.; Feng, Y.Z.; Li, C.L.; Lu, S. Late-stage southwards subduction of the Mongol-Okhotsk oceanic slab and implications for porphyry Cu Mo mineralization: Constraints from igneous rocks associated with the Fukeshan deposit, NE China. *Lithos* **2019**, *326–327*, 341–357. [CrossRef]
35. Hu, X.L.; Yao, S.Z.; He, M.C.; Ding, Z.J.; Cui, Y.B.; Shen, J.; Chen, B.; Zhu, B.P. Geochemistry, U–Pb Geochronology and Hf Isotope Studies of the Daheishan Porphyry Mo Deposit in Heilongjiang Province, NE China. *Resour. Geol.* **2014**, *64*, 102–116. [CrossRef]
36. Shang, Y.G.; Sun, F.Y.; Jiang, H.F.; Wang, Q.; Yin, Y.; Meng, Q.P.; Zhang, Z.Y. Petrogenesis of granodiorites in Huoluotai Cu–Pb–Zn mining area: Constrain from geochemistry and zircon U–Pb geochronology, northern Daxing'anling. *Glob. Geol.* **2017**, *36*, 474–485. (In Chinese) [CrossRef]

37. Sun, S.S.; McDonough, W.F. Chemical and isotopic systematics of oceanic basalts: Implications for mantle composition and processes. Magmatism in Ocean Basins. *Geol. Soc. Lond. Spec. Publ.* **1989**, *42*, 313–345. [CrossRef]
38. Wu, F.Y.; Li, X.H.; Zheng, Y.F.; Gao, S. Lu-Hf isotopic systematics and their applications in petrology. *Acta Petrol. Sin.* **2007**, *23*, 185–220. (In Chinese)
39. Diwu, C.R.; Sun, Y.; Lin, C.L.; Liu, X.M.; Wang, H.L. Zircon U-Pb ages and Hf isotopes and their geological significance of Yiyang gneisses from Henan province, China. *Acta Petrol. Sin.* **2007**, *23*, 253–262. (In Chinese)
40. Chappell, B.W.; White, A.J.R. I- and S-type granites in the Lachlan Fold Belt. *Earth Environ. Sci. Trans. R. Soc. Edinb.* **1992**, *83*, 1–26. [CrossRef]
41. Whalen, J.B.; Currie, K.L.; Chappell, B.W. A-type granites: Geochemical characteristics, discrimination and petrogenesis. *Contrib. Miner. Petrol.* **1987**, *95*, 407–419. [CrossRef]
42. Chappell, B.W. Aluminum saturation in I- and S-type granites and the characterization of fractionated haplogranites. *Lithos* **1999**, *46*, 535–551. [CrossRef]
43. Collins, W.J.; Beams, S.D.; White, A.J.R.; Chappell, B.W. Nature and origin of A-type granites with particular reference to southeastern Australia. *Contrib. Miner. Petrol.* **1982**, *80*, 189–200. [CrossRef]
44. El-Bialy, M.Z.; Abdel-Karim, A.; Azer, M. Petrogenesis of post-collisional granites in the Arabian-Nubian Shield: The peraluminous A-type granites of the mounts Um-Sudaydat and Um-Erjaj plutons, South Eastern Desert, Egypt. *Geochemistry* **2025**, *85*, 126346. [CrossRef]
45. Watson, E.B.; Harrison, T.M. Zircon saturation revisited: Temperature and composition effects in a variety of crustal magma types. *Earth Planet. Sci. Lett.* **1983**, *64*, 295–304. [CrossRef]
46. Wang, Q.; Zhao, Z.H.; Xiaong, X.L. The Ascertainment of Late-Yanshanian A-type Granite in Tongbai-Dabie Orogenic Belt. *Acta Petrol. Mineral.* **2000**, *19*, 297–306. (In Chinese)
47. Wu, F.Y.; Liu, X.C.; Ji, W.Q.; Wang, J.M.; Yang, L. Highly fractionated granites: Recognition and research. *Sci. China Earth Sci.* **2017**, *60*, 1201–1219. [CrossRef]
48. Clemens, J.D.; Stevens, G.; Farina, F. The enigmatic sources of I-type granites: The peritectic connexion. *Lithos* **2011**, *126*, 174–181. [CrossRef]
49. Chappell, B.W.; White, A.J.R. Two contrasting granite types: 25 years later. *Aust. J. Earth Sci.* **2001**, *48*, 489–499. [CrossRef]
50. Sun, J.Y.; Zheng, J.L.; Wei, X.Y.; Liu, J.S.; Cai, Y.L.; Guo, X.Y.; Wang, D.K.; Yang, Z.W. Zircon U–Pb age, geochemical characteristics and geological significance of Middle Jurassic granodiorite in Gaxiangou area, northern Great Xing'an Range. *J. Guilin Univ. Technol.* **2024**, *44*, 1–10. (In Chinese) [CrossRef]
51. Lin, Q.; Ge, W.C.; Wu, F.Y.; Sun, D.Y.; Cao, L. Geochemistry of Mesozoic granites in Da Hinggan Ling ranges. *Acta Petrol. Sin.* **2004**, *20*, 403–412. (In Chinese)
52. Wu, F.Y.; Sun, D.Y.; Lin, Q. Petrogenesis of the Phanerozoic granites and crustal growth in Northeast China. *Acta Petrol. Sin.* **1999**, *15*, 181–189. (In Chinese) [CrossRef]
53. Ballouard, C.; Poujol, M.; Boulvais, P.; Branquet, Y.; Tartèse, R.; Vigneresse, J.-L. Nb-Ta fractionation in peraluminous granites: A marker of the magmatic-hydrothermal transition. *Geology* **2016**, *44*, 231–234. [CrossRef]
54. Linnen, R.L.; Keppler, H. Melt composition control of Zr/Hf fractionation in magmatic processes. *Geochim. Cosmochim. Acta* **2002**, *66*, 3293–3301. [CrossRef]
55. Bau, M. Controls on the fractionation of isovalent trace elements in magmatic and aqueous systems: Evidence from Y/Ho, Zr/Hf and lanthanide tetrade effect. *Contrib. Miner. Petrol.* **1996**, *123*, 323–333. [CrossRef]
56. Chen, J.Y.; Yang, J.H. Petrogenesis of the Fogang highly fractionated I-type granitoids: Constraints from Nb, Ta, Zr and Hf. *Acta Petrol. Sin.* **2015**, *31*, 846–854. (In Chinese)
57. Shi, L.; Zheng, C.Q.; Yao, W.G.; Li, J.; Xu, J.L.; Gao, Y.; Cui, F.H. Geochronology, petro-geochemistry and tectonic setting of the Hamagou forest farm A-type granites in the Wuchagou region, Central Great Xinggan Range. *Acta Geol. Sin.* **2013**, *87*, 1264–1276. (In Chinese) [CrossRef]
58. Ge, W.C.; Wu, F.Y.; Zhou, C.Y.; Zhang, J.H. Metallogenic Epoch and Its Geodynamic Significance of Porphyry Cu-Mo Deposits in the Eastern Edge of Xing-Meng Orogenic Belt. *Chin. Sci. Bull.* **2007**, *52*, 2407–2417. (In Chinese)
59. Yang, J.H.; Wu, F.Y.; Liu, X.M.; Xie, L.W. Zircon U-Pb ages and Hf isotopes and their geological significance of the Miyun rapakivi granites from Beijing, China. *Acta Petrol. Sin.* **2005**, *21*, 1633–1644. (In Chinese)
60. Han, B.F.; Wang, S.G.; Jahn, B.M.; Hong, D.W.; Kagami, H.; Sun, Y.L. Depleted-mantle source for the Ulungur River A-type granites from North Xinjiang, China: Geochemistry and Nd–Sr isotopic evidence, and implications for Phanerozoic crustal growth. *Chem. Geol.* **1997**, *138*, 135–159. [CrossRef]
61. Rapp, R.P.; Shimizu, N.; Norman, M.D.; Applegate, G.S. Reaction between slab-derived melts and peridotite in the mantle wedge: Experimental constraints at 3.8 GPa. *Chem. Geol.* **1999**, *160*, 335–356. [CrossRef]
62. Rudnick, R.L.; Fountain, D.M. Nature and Composition of the Continental Crust: A Lower Crustal Perspective. *Rev. Geophys.* **1995**, *33*, 267–309. [CrossRef]

63. Rapp, R.P.; Watson, E.B. Dehydration Melting of Metabasalt at 8-32 kbar: Implications for Continental Growth and Crust-Mantle Recycling. *J. Petrol.* **1995**, *36*, 891–931. [CrossRef]
64. Rudnick, R.L.; Gao, S. Composition of the continental crust. In *The Crust, Treatise on Geochemistry*; Holland, H.D., Turekian, K.K., Eds.; Elsevier-Pergamon: Oxford, UK, 2014; pp. 1–51.
65. Zhang, Z.Z.; Gu, L.X.; Wu, C.Z.; Zhai, J.P.; Li, W.Q.; Tang, J.H. Weiya quartz syenite in early Indosinina from eastern Tianshan Mountains: Petrogenesis and tectonic implications. *Acta Petrol. Sin.* **2006**, *22*, 1135–1149. (In Chinese)
66. Moyen, J.F. High Sr/Y and La/Yb ratios: The meaning of the "adakitic signature". *Lithos* **2010**, *112*, 556–574. [CrossRef]
67. Smithies, R.H.; Champion, D.C. The Archaean High-Mg Diorite Suite: Links to Tonalite-Trondhjemite-Granodiorite Magmatism and Implications for Early Archaean Crustal Growth. *J. Petrol.* **2000**, *41*, 1653–1671. [CrossRef]
68. Ge, W.C.; Sui, Z.M.; Wu, F.Y.; Zhang, J.H.; Xu, X.C.; Cheng, R.Y. Zircon U-Pb ages, Hf isotopic characteristics and their implications of the Early Paleozoic granites in the northeastern Da Hinggan Mts., northeastern China. *Acta Petrol. Sin.* **2007**, *23*, 423–440. (In Chinese)
69. Hong, D.W.; Wang, S.G.; Xie, X.L.; Zhang, J.S. Genesis of positive εNd(t) granitoids in the Da Hinggan Mts. Mongolia orogenic belt and growth continental crust. *Earth Sci. Front.* **2000**, *7*, 441–456. (In Chinese)
70. Donskaya, T.V.; Gladkochub, D.P.; Mazukabzov, A.M. Late Paleozoic—Mesozoic subduction-related magmatism at the southern margin of the Siberian continent and the 150 million-year history of the Mongol-Okhotsk Ocean. *J. Asian Earth Sci.* **2013**, *62*, 79–97. [CrossRef]
71. Wang, T.; Guo, L.; Zhang, L.; Yang, Q.D.; Zhang, J.J.; Tong, Y.; Ye, K. Timing and evolution of Jurassic–Cretaceous granitoid magmatisms in the Mongol–Okhotsk belt and adjacent areas, NE Asia: Implications for transition from contractional crustal thickening to extensional thinning and geodynamic settings. *J. Asian Earth Sci.* **2015**, *97*, 365–392. [CrossRef]
72. Tang, J.; Xu, W.L.; Wang, F.; Ge, W.C. Subduction history of the Paleo-Pacific slab beneath Eurasian continent: Mesozoic-Paleogene magmatic records in Northeast Asia. *Sci. China Earth Sci.* **2018**, *61*, 527–559. [CrossRef]
73. Tang, J.; Xu, W.L.; Wang, F.; Zhao, S.; Li, Y. Geochronology, geochemistry, and deformation history of Late Jurassic–Early Cretaceous intrusive rocks in the Erguna Massif, NE China: Constraints on the late Mesozoic tectonic evolution of the Mongol–Okhotsk orogenic belt. *Tectonophysics* **2015**, *658*, 91–110. [CrossRef]
74. Li, Z.M.; Shi, S.S.; Li, Y.H.; Wang, Y.L.; Shi, J.M.; Jiang, S. Zircon U-Pb dating and geochemistry of the volcanic rocks of Tamulangou formation in the south edge of Mohe basin: Geological implication. *Geol. Resour.* **2015**, *24*, 526–531. (In Chinese) [CrossRef]
75. Li, B.L.; Sun, Y.G.; Chen, G.J.; Xi, A.H.; Zhi, Y.B.; Chang, J.J.; Peng, B. Zircon U-Pb geochronology, geochemistry and Hf isotopic composition and its geological implication of the fine-grained syenogranite in Dong'an goldfield from the Lesser Xing'an Mountains. *Earth Sci.* **2016**, *41*, 1–16. (In Chinese) [CrossRef]
76. Chen, Y.J.; Zhang, C.; Wang, P.; Pirajno, F.; Li, N. The Mo deposits of Northeast China: A powerful indicator of tectonic settings and associated evolutionary trends. *Ore Geol. Rev.* **2017**, *81*, 602–640. [CrossRef]
77. Li, Z.Z.; Qin, K.Z.; Li, G.M.; Ishihara, S.; Jin, L.Y.; Song, G.X.; Meng, Z.J. Formation of the giant Chalukou porphyry Mo deposit in northern Great Xing'an Range, NE China: Partial melting of the juvenile lower crust in intra-plate extensional environment. *Lithos* **2014**, *202–203*, 138–156. [CrossRef]
78. Nie, F.J.; Sun, Z.J.; Li, C.; Liu, Y.F.; Lv, K.P.; Zhang, K.; Liu, Y. Re-Os isotopic dating of molybdenite separates from Chalukou porphyry Mo polymetallic deposit in Heilongjiang Province. *Miner. Depos.* **2011**, *30*, 828–836. (In Chinese)
79. She, H.Q.; Li, J.W.; Xiang, A.P.; Guan, J.D.; Yang, X.C.; Zhag, D.Q.; Tan, G.; ZHang, B. U–Pb ages of the zircons from primary rocks in middle–northern Daxinganling and its implications to geotectonic evolution. *Acta Petrol. Sin.* **2012**, *28*, 571–594. (In Chinese)
80. Sun, R.J.; Sun, D.Y.; Gou, J.; Wang, G.T.; Yang, D.G.; Li, X. Geochemical characteristics and petrogenesis of adamellite-granite in Xinlin Town, northern Da Hinggan Mountains. *Glob. Geol.* **2016**, *35*, 309–323. (In Chinese) [CrossRef]
81. Wang, L. Study on geological characteristics and prospecting direction of Huoluotai copper-molybdenum deposit in Mohe County, Heilongjiang Province. Master's Thesis, Jilin University, Changchun, China, 2018. (In Chinese)
82. Wang, W.D.; Yang, H.B.; Liu, T.; Ma, Z.Z.; Zheng, J.L.; Hu, J.H.; Wei, X.Y. Chronology, geochemistry and tectonic implications of Early Cretaceous igneous rocks in Xinlin Zhanbeicun area, northern Great Hinggan Mountain. *Glob. Geol.* **2018**, *37*, 21–36. (In Chinese) [CrossRef]
83. Yang, X.P.; Hu, D.G.; Liu, X.J.; Zhang, W.L.; Wang, Y.; Wang, C.Q. LA–MC–ICP–MS Zircon U–Pb Ages of Kaikukang Formation and Their Tectonic Implications in Mohe Basin, Northeast China. *J. Earth Sci. Environ.* **2018**, *40*, 237–251. (In Chinese)
84. Yu, C.W. Geochronology and Geochemistry of the Early Cretaceous Intrusion in the Northeastern Tahe, Northern Dahinggan Mountain. Master's Thesis, China University of Geosciences (Beijing), Beijing, China, 2018. (In Chinese)
85. Ma, Y.B.; Zhang, Y.; Li, L.X.; Xing, S.W.; Zhang, Z.J.; Zhang, T.; Xiao, K.Y.; Wang, H.P.; Fan, J.P. Re–Os isotope age of pyrite and He–Ar isotope of sulfides from the Biliyagu Pb–Zn deposit in the northern Great Xing'an Range. *Acta Geol. Sin.* **2022**, *96*, 1265–1278. (In Chinese) [CrossRef]
86. Nie, F.J.; Zhang, W.Y.; Du, A.D.; Jiang, S.H.; Liu, Y. Re-Os Isotopic Age Dating of Molybdenite Separates from the Chaobuleng Skarn Iron-Polymetallic Deposit, Dong Ujimqin Banner, Inner Mongolia. *Acta Geosci. Sin.* **2007**, *28*, 315–323. (In Chinese)

87. Liu, J.; Wu, G.; Qiu, H.N.; Gao, D.Z.; Yang, X.S. $^{40}Ar/^{39}Ar$ Dating of Gold-Bearing Quartz Vein from the Shabaosi Gold Deposit at the Northern End of the Great Xing'an Range and Its Tectonic Significance. *Acta Geol. Sin.* **2013**, *87*, 1570–1579. (In Chinese) [CrossRef]
88. Zhang, S.; Lin, C.M.; Wu, C.D.; Yang, J.G. Tectonic Characteristics and Basin Evolution of the Mohe Basin, Heilongjiang Province. *Geol. J. China Univ.* **2003**, *9*, 411–419. (In Chinese)
89. Yang, Y.J.; Yang, X.P.; Jiang, B.; Wang, Y.; Pang, X.J. Spatio-temporal distribution of Mesozoic volcanic strata in the Great Xing'an Range: Response to the subduction of the Mongol–Okhotsk Ocean and Paleo-Pacific Ocean. *Earth Sci. Front.* **2022**, *29*, 115–131. (In Chinese) [CrossRef]
90. Gao, X.R.; Liang, C.Y.; Zheng, C.Q.; Liu, Y.J.; Zhou, J.B.; Song, Z.W.; Jia, X.H.; Yin, J.Z.; Hong, Y.X.; Tan, Z.; et al. Late Mesozoic Evolution History of Eastern Section of Mongol-Okhotsk Tectonic Domain: Evidence from Igneous and Sedimentary Rocks. *J. Jilin Univ. (Earth Sci. Ed.)* **2026**, *56*, 36–65. (In Chinese) [CrossRef]
91. Sun, Q.S.; Fang, S.; Xie, R.X.; Gong, F.H.; Li, S.C.; Zhu, H.; Yuan, W. The application of zircon fission track to the study of the up-lifting process in the Mohe Basin. *Geol. Bull. China* **2016**, *35*, 807–813. (In Chinese)
92. Yang, X.P.; Wang, C.B.; Li, W.Q. Petrogenesis and Tectonic Setting of Moyite in Suotuhan Area, Northern Great Xing'an Range. *J. Jilin Univ. (Earth Sci. Ed.)* **2019**, *49*, 1338–1349. (In Chinese) [CrossRef]
93. Pearce, J.A.; Harris, N.B.W.; Tindle, A.G. Trace Element Discrimination Diagrams for the Tectonic Interpretation of Granitic Rocks. *J. Petrol.* **1984**, *25*, 956–983. [CrossRef]
94. Zhang, J.H.; Gao, S.; Ge, W.C.; Wu, F.Y.; Yang, J.H.; Wilde, S.A.; Li, M. Geochronology of the Mesozoic volcanic rocks in the Great Xing'an Range, northeastern China: Implications for subduction-induced delamination. *Chem. Geol.* **2010**, *276*, 144–165. [CrossRef]
95. Wang, F.; Zhou, X.H.; Zhang, L.C.; Ying, J.F.; Zhang, Y.T.; Wu, F.Y.; Zhu, R.X. Late Mesozoic volcanism in the Great Xing'an Range (NE China): Timing and implications for the dynamic setting of NE Asia. *Earth Planet. Sci. Lett.* **2006**, *251*, 179–198. [CrossRef]
96. Chen, L.; Liang, C.Y.; Neubauer, F.; Liu, Y.J.; Zhang, Q.; Song, Z.W. Sedimentary processes and deformation styles of the Mesozoic sedimentary succession in the northern margin of the Mohe basin, NE China: Constraints on the final closure of the Mongol–Okhotsk Ocean. *J. Asian Earth Sci.* **2022**, *232*, 105052. [CrossRef]

Disclaimer/Publisher's Note: The statements, opinions and data contained in all publications are solely those of the individual author(s) and contributor(s) and not of MDPI and/or the editor(s). MDPI and/or the editor(s) disclaim responsibility for any injury to people or property resulting from any ideas, methods, instructions or products referred to in the content.